

Modeling Frequency-Dependent Core Loss of Ferrite Materials Using Permeance–Capacitance Analogy for System-Level Circuit Simulations

Min Luo , Member, IEEE, Drazen Dujic , Senior Member, IEEE, and Jost Allmeling , Member, IEEE

Abstract—Ferrite core materials are preferred for magnetic components in power electronic converters considering their low cost and high permeability. Thanks to their negligible electrical conductivity, core loss is dominated by the frequency-independent hysteresis effect in most operating conditions. In the applications of high switching frequency under a certain modulation scheme, however, the core loss of ferrite materials do exhibit obvious frequency dependence, known as relaxation effect, which is strongly influenced by the magnetic flux’s rate of change and cannot be ascribed to material conductivity. In order to incorporate the core loss including both frequency-dependent and frequency-independent effects into system-level simulation environment of power converters so that the system efficiency can be pre-evaluated during the design phase as a reference for optimization, dynamic model that is physically intuitive and easy to parameterize is desired. This paper proposes an approach to model the core loss of ferrite materials combining both frequency-dependent relaxation effect and frequency-independent hysteresis, which can be flexibly applied for various operation conditions with good accuracy.

Index Terms—Core loss, ferrite material, frequency dependent, magnetic circuit, permeance–capacitance.

NOMENCLATURE

B	Flux density.
H	Field strength.
F	Magnetomotive force.
Φ	Magnetic flux.
\mathcal{P}	Magnetic permeance.
μ	Magnetic permeability.

I. INTRODUCTION

FERRITE is a popular type of core material to produce magnetic components in power electronic applications, taking advantage of its low cost and relatively high permeability.

Manuscript received March 25, 2018; revised May 6, 2018; accepted June 29, 2018. Date of publication July 10, 2018; date of current version February 20, 2019. This work was supported in the frame of the ECPE Joint Research Programme. Recommended for publication by Associate Editor M. Duffy. (*Corresponding author: Min Luo*)

M. Luo and D. Dujic are with the Power Electronics Laboratory, École Polytechnique Fédérale de Lausanne, Lausanne CH-1015, Switzerland (e-mail: min.luo@epfl.ch; drazen.dujic@epfl.ch).

J. Allmeling is with the Plexim GmbH, Zürich CH-8005, Switzerland (e-mail: allmeling@plexim.com).

Color versions of one or more of the figures in this paper are available online at <http://ieeexplore.ieee.org>.

Digital Object Identifier 10.1109/TPEL.2018.2854874

In order to predict the overall efficiency and determine the cooling condition, core loss of the ferrite-based magnetic components need to be estimated during the design phase of the power converters. In general, the core loss of magnetic materials can be separated into following three parts according to [1].

- 1) Hysteresis loss: Frequency-independent effect related to the material nonlinearity.
- 2) Eddy current loss: Frequency-dependent effect related to the material conductivity.
- 3) Relaxation loss: Frequency-dependent effect related to other physical mechanisms.

Due to the low electrical conductivity, eddy current, which is obviously taking place in metal-based core materials (e.g., silicon steel), is negligible in ferrites, so that the core loss is dominated by the frequency-independent hysteresis effect in most operating conditions of power converters. However, in high-frequency (e.g., >20 kHz) applications under certain modulation schemes, the core loss of ferrite materials do exhibits strong frequency and rate dependencies, which cannot be ascribed to eddy current but the relaxation effect.

In practice, the core loss is usually estimated using empirical formulas based on Steinmetz equation (SE), whose parameters are extracted from experimental measurements under sinusoidal excitation. Reinert *et al.* [2] proposed an improved form of SE (iGSE) to generalize it to nonsinusoidal excitations, as is the case in power electronic applications. In [3], Sullivan *et al.* have observed that under phase-shift modulation (e.g., in the case of galvanically isolated type of dc–dc converters shown in Fig. 1), where a zero-voltage period is present, and strongly asymmetrical pulsewidth modulation (PWM) with duty cycle far away from 50%, the core loss increases significantly in comparison to the case of 50% symmetrical PWM. In the aforementioned modulation schemes, Muehlethaler *et al.* [4] have demonstrated that the improved form proposed by Reinert *et al.* [2] still significantly underestimated the core loss. Aiming to reduce the error, an additional term has been added to the iGSE, resulting in improved-improved generalized SE. Alternatively, the approach based on the composite waveform hypothesis proposed by Sullivan *et al.* [3] was further developed by Barg *et al.* [5]. Physically, this considerable relaxation loss under high switching frequency PWM excitation with zero-voltage period or strongly asymmetrical duty cycle takes place if the thermal equilibrium of a magnetic system is suddenly altered by some

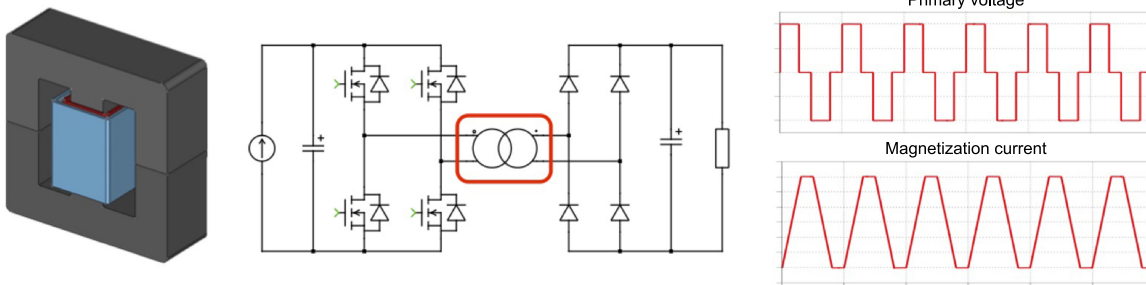


Fig. 1. Isolation transformer in a dc–dc converter with phase-shift modulation and the typical operational waveforms of primary voltage and magnetization current.

external force and the re-establishment of a new thermal equilibrium happens progressively, as introduced in the work of Goodenough [1]. More detailed analysis of relaxation effect can be found in [6].

Although the continuously improved empirical equations proposed by the existing publications provide even better accuracy in core loss estimation, the physics behind it are still obscure and unintuitive for power electronic engineers, who are not researching deeply in the area of magnetics. In the design phase of power converters, to help engineers with understanding the physical interaction between the components and evaluating the dynamic behavior of the whole system, time-domain circuit simulation is commonly adopted. The empirical equations, however, are difficult to be incorporated into the circuit simulation environment. In order to reflect the core loss's impact on the dynamic behavior of the converter system, Abramovitz and Ben-Yaakov [7] managed to interpret iGSE directly into SPICE-type circuit simulator via a variable resistor, which achieved good accuracy in various operating conditions. However, the loss mechanism still remains as a black box having the same transparency level as the empirical equation, where all the three loss components (hysteresis, eddy current, and relaxation) are mixed together.

To provide a clear insight of the loss mechanism, it is desired to present the loss components separately in the simulation environment. Frequency-independent hysteresis loss can be exclusively represented in time domain by a classical Preisach model in a flexible way [8]. In the work presented in [9] and [10], the classical Preisach model is extended in circuit simulation for static hysteresis effect of ferrite materials, where good accuracy was achieved in various excitation amplitudes. Beside using a Preisach model for frequency-independent hysteresis, the other two loss components—eddy current and residual effect—are incorporated by Zhu *et al.* [11] via introducing two resistive components. However, the model was only verified under symmetrical PWM excitation without zero-voltage period, where the relaxation loss hardly has visible impact, whereas the eddy current loss is intrinsically negligible in ferrite materials. van Vlerken and Blanken [12] modeled the relaxation effect explicitly by using a third-order circuit model, and the similar model structure was also applied later by Dalessandro *et al.* [13], whereas the frequency-independent hysteresis effect was not taken into account and the fidelity is verified in frequency response rather than time domain.

Aiming to provide a model that is sufficiently accurate to capture the total core loss of ferrite materials and is meanwhile clear

and intuitive enough in terms of the individual loss mechanism, the modeling approach proposed by this paper differs from the existing publications in the following aspects.

- 1) The frequency-dependent relaxation effect is specifically modeled. An explicit way of parameterization from measurement result is introduced.
- 2) The frequency-independent hysteresis effect is also individually covered using the Preisach model and combined in the same circuit structure.
- 3) The total core loss is physically present in the circuit model, whereas the mechanism of individual loss components (hysteresis and relaxation) can be clearly investigated.
- 4) The permeance-capacitor-based magnetic circuit proposed by Hamill [14] and further adopted in the research works presented in [10] and [15] is chosen as the fundamental platform, which has seamless interface to an electrical circuit. In the permeance magnetic circuit, the relaxation effect can be explained in an intuitive way, as will be presented in the following sections.

In Section II, the experimental result of the operating condition, where both frequency-independent hysteresis and frequency-dependent relaxation effect are obviously visible, is presented. In Section III, referring to the experimental result, the fundamental model structure and physical origins of the frequency-dependent relaxation effect is interpreted into a permeance-magnetic circuit, as the starting point of the modeling. The parameterization process of the proposed model for ferrite material and the required measurement data are introduced in Section IV. Afterward in Section V, the proposed model is verified by the experimental test of different ferrite materials under various operating conditions including switching frequency, duty cycle, and zero-voltage period. At the end, summary and outlook are provided in Section VI.

II. EXPERIMENTAL MEASUREMENT

A. Test Setup

For material characterization and model verification purpose, a multifunctional magnetic characterization test setup has been constructed, which is able to provide both low-frequency

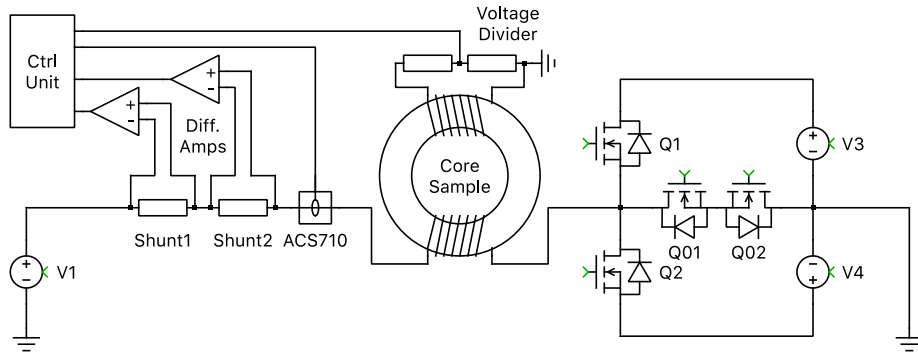


Fig. 2. Circuit schematic of the test setup.

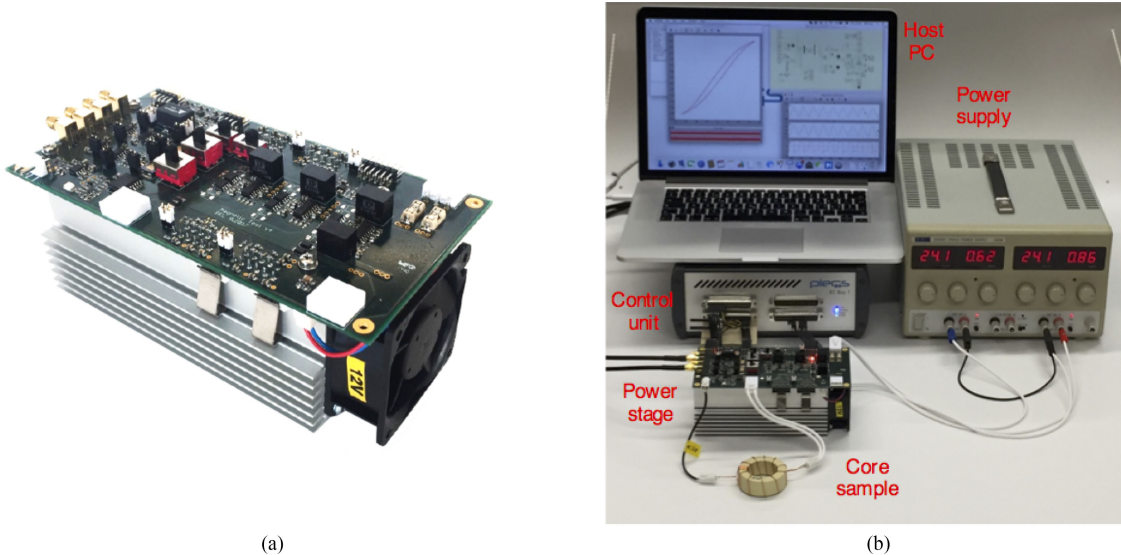


Fig. 3. (a) Power stage hardware of the test setup. (b) Complete configuration of the test setup including the power stage, core sample, power supply, control unit (PLECS RT-Box), and host PC.

sinusoidal and high-frequency PWM excitations. The hardware of the characterization setup is designed to have 24 V rated output voltage and 6 A rated output current. The basic idea is derived from the $V-I$ approach proposed by the work of Tan *et al.* [16]. The circuit schematic and photo of a actual setup are shown in Fig. 2 and Fig. 3, and include the following elements.

- 1) Controlled voltage source V_1 : Realized using a power amplifier of type LM3886 with 2 MHz gain bandwidth product and is supplied by ± 24 V. The main usage is to generate sinusoidal excitation.
- 2) Single phase T-type bridge: Composed of three MOSFET switches (pairs) (Q_{01} and Q_{02} , Q_1 , and Q_2) to generate three-level PWM excitation. Both Q_1 and Q_2 are connected to controlled voltage sources (V_3 and V_4) that are realized using the same type of power amplifier as V_1 .
- 3) Core sample: Following the $V-I$ approach for magnetic material characterization, the core sample is equipped with two windings as demonstrated in Fig. 2. The primary winding is excited by the power stage whose current is measured to obtain field strength H . The secondary

winding is left open, the voltage of which is measured and integrated in time domain to obtain flux density B .

- 4) Current measurement: Realized using a low-inductance shunt resistor. The voltage drop of the shunt resistor is sensed and amplified using differential instrumentation amplifiers. Two sets of shunt resistors' (different resistances) circuitry are mounted to achieve different resolutions of measurement.
- 5) Voltage measurement: Realized using a low-capacitance resistive voltage divider. The scaled voltage is buffered and amplified by an operational amplifier with 180-MHz bandwidth.
- 6) Control unit: One PLECS RT-Box is deployed as a control unit for the test setup, which is graphically operated by a host personal computer (PC).

B. Measurement Results

To demonstrate the impact of the relaxation effect at high switching frequency excitation, comparative measurement has been carried out based on the ferrite material N87 from EP-COS, with the toroidal core of size code "R 20.0 \times 10.0 \times

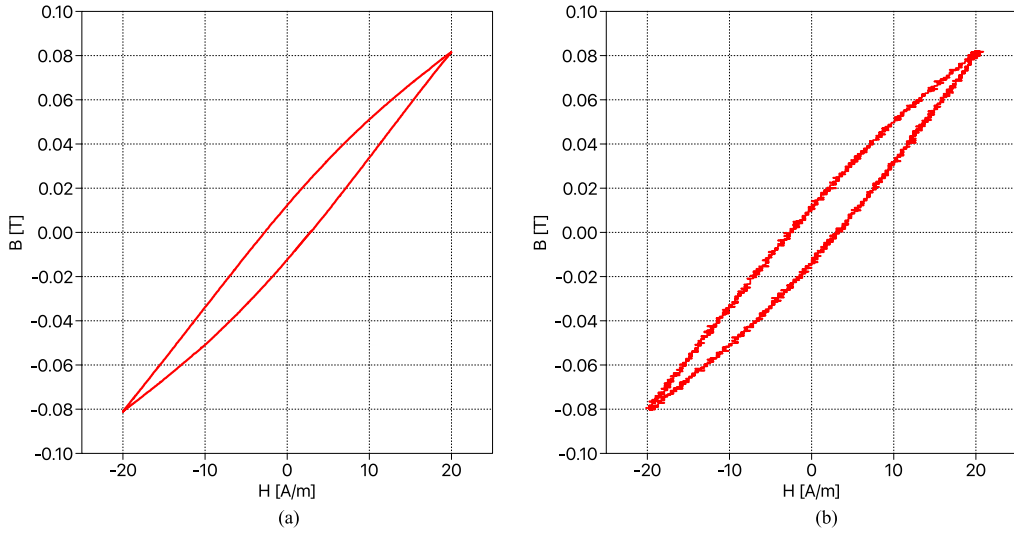


Fig. 4. Measured B - H characteristic of ferrite N87 with peak strength $\hat{H} = 20$ A/m excited by (a) 500-Hz sinusoidal excitation. (b) 50-kHz symmetrical PWM excitation without zero-voltage period.

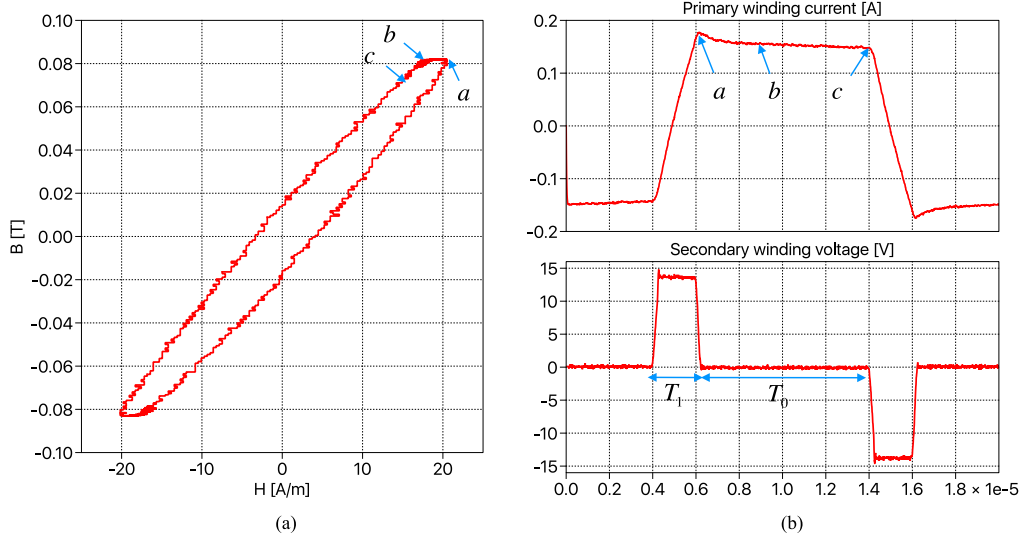


Fig. 5. Measurement results of ferrite N87 (peak strength $\hat{H} = 20$ A/m) excited by 50-kHz symmetrical PWM excitation with zero-voltage period of $T_0 = 8 \mu\text{s}$. (a) B - H characteristic. (b) Primary winding current and secondary winding voltage.

7.00" chosen as sample. The turns number of both windings are $N_1 = N_2 = 5$. As the temperature dependence is not in the scope of this work, all tests for parameterization and verification have been conducted under room temperature of 25 °C.

At first, the core sample is excited by sinusoidal excitation generated from the controlled voltage source V_1 (with switches Q_{01} and Q_{02} closed and Q_1 and Q_2 open) and the frequency is configured to be 500 Hz where the frequency-dependent effect is negligible. The amplitude of V_1 is adjusted to generate a B - H loop with peak field strength $\hat{H} = 20$ A/m, as shown in Fig. 4(a). Second, the test setup is reconfigured to provide 50-kHz symmetrical PWM excitation without zero-voltage period, where the switches Q_{01} and Q_{02} are open and Q_1 and Q_2 actively switched. The output of the voltage sources V_3 and V_4 are provided by the reference signal with the same

amplitude but opposite polarity, which is adjusted to generate a B - H loop with peak field strength $\hat{H} = 20$ A/m, as shown in Fig. 4(b) (V_1 is tuned to ensure zero dc bias). Comparing Fig. 4(a) and Fig. 4(b), only slight shape difference can be detected, whereas the per-cycle energy loss (indicated by the loop area) exhibits less than 10% difference. This indicates that the part of frequency-independent core loss still dominates in this operating condition although the switching frequency 50 kHz is significantly higher than 500 Hz.

Afterward, a zero-voltage period of duration $t_0 = 8 \mu\text{s}$ is inserted into the PWM excitation with the midpoint switches Q_{01} and Q_{02} activated, the voltage output of V_3 and V_4 are adjusted to ensure that the peak amplitude is still equal to $\hat{H} = 20$ A/m. The measured B - H characteristic and time-domain primary current and secondary voltage are shown in Fig. 5(a) and (b),

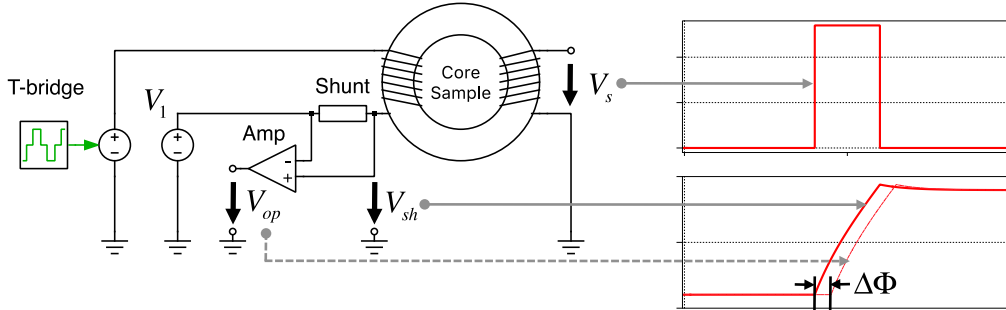


Fig. 6. Phase error compensation of the differential amplifier output in the current measurement.

respectively. In comparison to Fig. 4, significantly larger B - H loop area can be observed especially in the location approaching the peak. The flat part between the points “a” and “b” arises from the relaxation effect, where the field strength decreases although nearly zero excitation is applied, as has also been observed in the work of Muehlethaler *et al.* [4]. According to the observed phenomenon, the basic model structure of the relaxation effect is derived using permeance-capacitor-based magnetic circuit in the next section.

C. Discussion of Measurement Accuracy

During measurement and data post processing, one should pay attention to the influence of the phase error between the current and voltage. Tan *et al.* [16] have explored that the percentage error of the core loss power can be expressed as follows:

$$\Delta\% = \tan(\Phi_{v-i}) \cdot \Delta\Phi \quad (1)$$

where Φ_{v-i} is the absolute phase shift between the measured primary winding current and second winding voltage under sinusoidal excitation, whereas $\Delta\Phi$ is the error of the phase shift arising from the measurement system. Equation (1) indicates that the closer to 90° is Φ_{v-i} the more sensitive is the percentage error to $\Delta\Phi$. Different modifications on the measurement circuit structure have been proposed in [17], [19], so as to drag Φ_{v-i} away from 90° and thus decreases the sensitivity to $\Delta\Phi$. There high excitation frequency of several or tens of MHz was discussed, and the frequency in this paper (50 kHz), however, is far below that range. Considering the fact that $\Delta\Phi$ is proportional to the excitation frequency [20], the influence of $\Delta\Phi$ is significantly lower in the frequency range of this paper. Moreover, with the modification although the core loss power can be more accurately measured, the exact shape of B - H is not available anymore, which, however, is necessary for the model parameterization and verification in this paper. Therefore, the original circuit structure from [16] is still adopted.

The influence of phase error in the measurement of low-frequency (500 Hz) sinusoidal excitation can be neglected. For the case of 50-kHz PWM excitation, phase error compensation has been applied in postprocessing. Phase error may exist in both voltage and current measurements.

- 1) Voltage measurement: In the 50 kHz measurement, due to the sufficiently large amplitude of the excitation voltage, the amplification stage is bypassed. The secondary

winding is directly connected to the oscilloscope via shielded axial cable (V_s in Fig. 6), which has the same length as that of the current measurement, so that the phase delay of the voltage measurement can be neglected.

- 2) Current measurement: According to the datasheet of the ferrite material N87 [21], the per-volume core loss (25°C) at frequency $f = 50$ kHz and peak-to-peak flux density $\Delta B = 200$ mT (amplitude 100 mT) is 54 kW/m 2 , which corresponds to $P_{\text{loss}} = 0.08$ W loss power for the core “R $20.0 \times 10.0 \times 7.00$,” if multiplied by the core volume. The equivalent phase shift between voltage and current can be calculated as follows [20]:

$$\Phi_{v-i} = \arctan \left(\frac{(N_1 \cdot A \cdot 2\pi f \cdot \Delta B)^2}{8 \cdot P_{\text{loss}}} \cdot \frac{1}{2\pi f \cdot L} \right). \quad (2)$$

In the above equation, $\Phi_{v-i} = 84.6^\circ$, where $N_1 = 5$ is the primary winding turns number, A is the cross-sectional area of the core and L the equivalent inductance calculated from the A_L value provided by the manufacturer’s datasheet [21].

If we target $\epsilon_{\text{ph}} = \pm 5\%$ phase error in (1), the allowed uncompensated phase error is $\pm 0.272^\circ$ at 50 kHz. The first source of the uncompensated phase error is the sample step size of the oscilloscope, which is in our case equal to 10 ns (0.18° for 50 kHz). The second source of the uncompensated phase error arises from the stray inductance of the shunt resistor. The manufacturer of the 0.1Ω shunt resistor [22] specifies that the stray inductance is typically 0.5 nH, which results in a phase angle of 0.09° at 50 kHz. The sum of the phase error of the oscilloscope and shunt resistor is within the criteria 0.272° .

The differential amplifier aims to filter out electromagnetic compatibility noise and eliminate the dc voltage bias of the power amplifier V_1 , and the phase delay between the voltage drop on the shunt resistor and the differential amplifier’s output can be explicitly compensated: as demonstrated in the simplified circuit schematic shown in Fig. 6, for each measurement, voltage V_{sh} between the positive terminal of the shunt and ground (with dc bias of V_1) is connected to the oscilloscope using a coaxial cable with the same length as the differential amplifier’s output V_{op} (without dc bias of V_1).

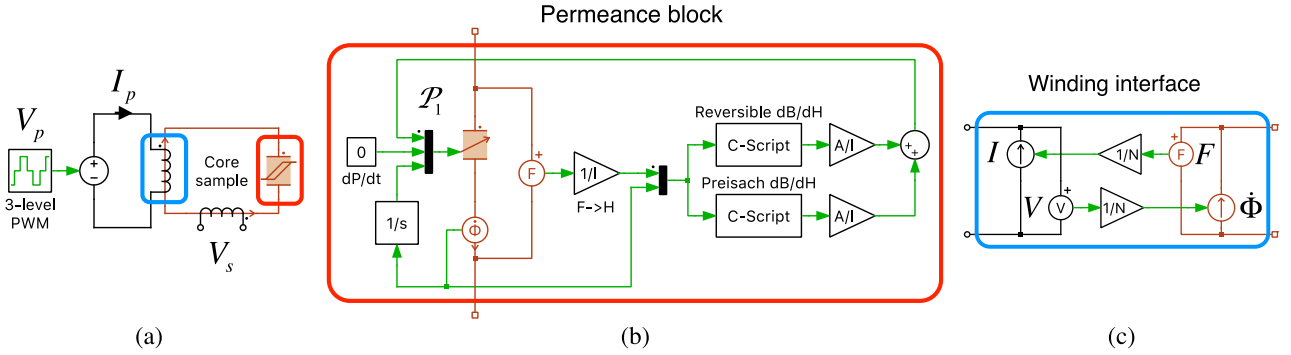


Fig. 7. (a) Simplified model of the test setup including both electrical and magnetic circuits. (b) Internal structure of the permeance block. (c) Winding interface using a gyrator structure.

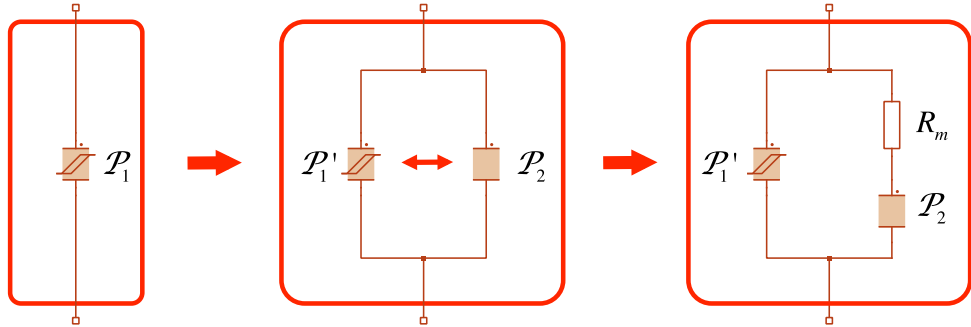


Fig. 8. Modification of the original hysteresis permeance block to incorporate the relaxation effect, where the permeance value of \mathcal{P}'_1 is provided by subtracting \mathcal{P}_2 from \mathcal{P}_1 .

At the moment when the excitation voltage becomes positive from zero, the time difference between the turning point of V_{sh} and that of V_{op} is considered as the phase delay $\Delta\Phi$ to be compensated (with the uncompensated phase error discussed previously). During the data post-processing to calculate core loss, the current measurement should be shifted by $-\Delta\Phi$. For the measurement of other materials and cores, compensation is applied following similar consideration.

Besides the phase error, the equipment accuracy also adds up to the measurement error, which can be found in the datasheet of the corresponding components and devices. The major contribution comes from the following.

- 1) The shunt resistor has an error of $\epsilon_{sh} = \pm 0.5\%$.
 - 2) The chip resistor to configure the gain of the differential amplifier has $\epsilon_{amp} = 0.1\%$ error.
 - 3) The oscilloscope has a measurement error of $\epsilon_{osc} = \pm 2\%$.
- Combining these three error sources and the phase error together, the system measurement error is calculated by

$$\epsilon_{sys} = (1 + \epsilon_{sh}) \cdot (1 + \epsilon_{amp}) \cdot (1 + \epsilon_{osc}) \cdot (1 + \epsilon_{ph}) - 1. \quad (3)$$

The above equation yields $\epsilon_{sys} = \pm 7.7\%$.

III. PROPOSED MODEL

A. Model Behavior

The model for the frequency-independent hysteresis effect introduced in [10] is taken as the starting point for the modeling

approach in this paper. The equivalent electric-magnetic circuit of the test setup is demonstrated in Fig. 7(a), which includes the PWM excitation represented by a voltage source, the winding block as interface to magnetic circuit [see Fig. 7(b)], and the permeance building block modeling the core sample. The internal structure of the permeance block, which is able to represent a complete magnetic core of simple geometry or one part of that with complex geometry, is demonstrated in Fig. 7(c). Please note that in the work of [10], two variable permeance blocks accounting for irreversible and reversible magnetizations are connected in parallel for illustration purpose, whereas in this paper, they are structurally merged into one and the differential permeability of the irreversible and reversible components are summed up as $\mathcal{P}_1(H)$, which is physically equivalent to that in [10].

After the parameters of the formula in calculating $\mathcal{P}_1(H)$ are completely identified using the experimental measurement at low-frequency sinusoidal excitation, as has been described by Luo *et al.* [10], the relaxation effect can be incorporated. As illustrated in Fig. 8, at first, the permeance block \mathcal{P}_1 is split into two permeance blocks in parallel, namely \mathcal{P}'_1 and \mathcal{P}_2 . It is first assumed that the permeance \mathcal{P}_2 is constant

$$\mathcal{P}'_1(H) = \mathcal{P}_1(H) - \mathcal{P}_2. \quad (4)$$

Second a “magnetic” resistor R_m is connected to the branch of \mathcal{P}_2 . Similar to the behavior of a nelectrical resistor, the “magnetic” voltage drop [magnetomotive force (MMF) F] across R_m is equal to R_m multiplied by the “magnetic” current (flux

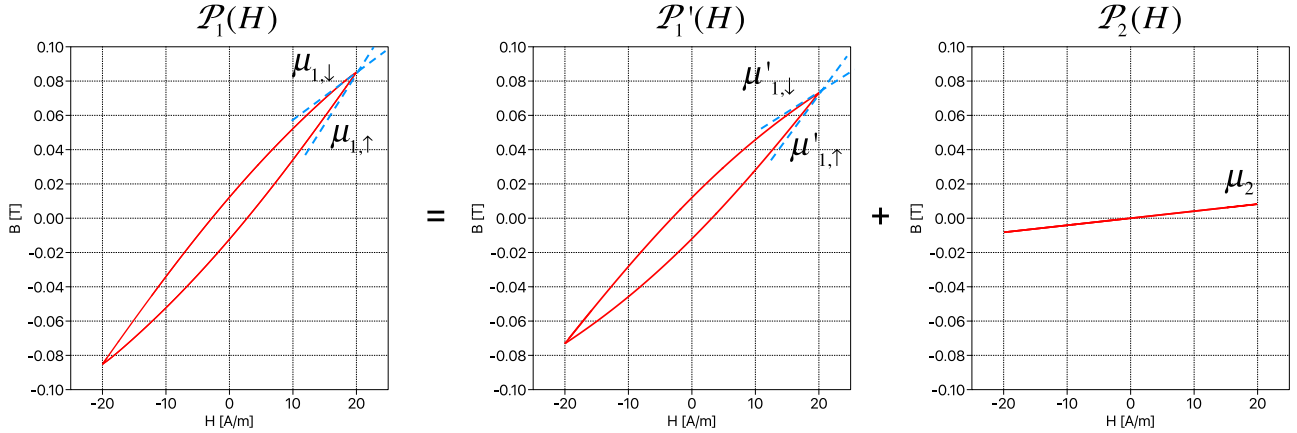


Fig. 9. Summation of the B - H characteristic of P'_1 and P_2 under low-frequency excitation.

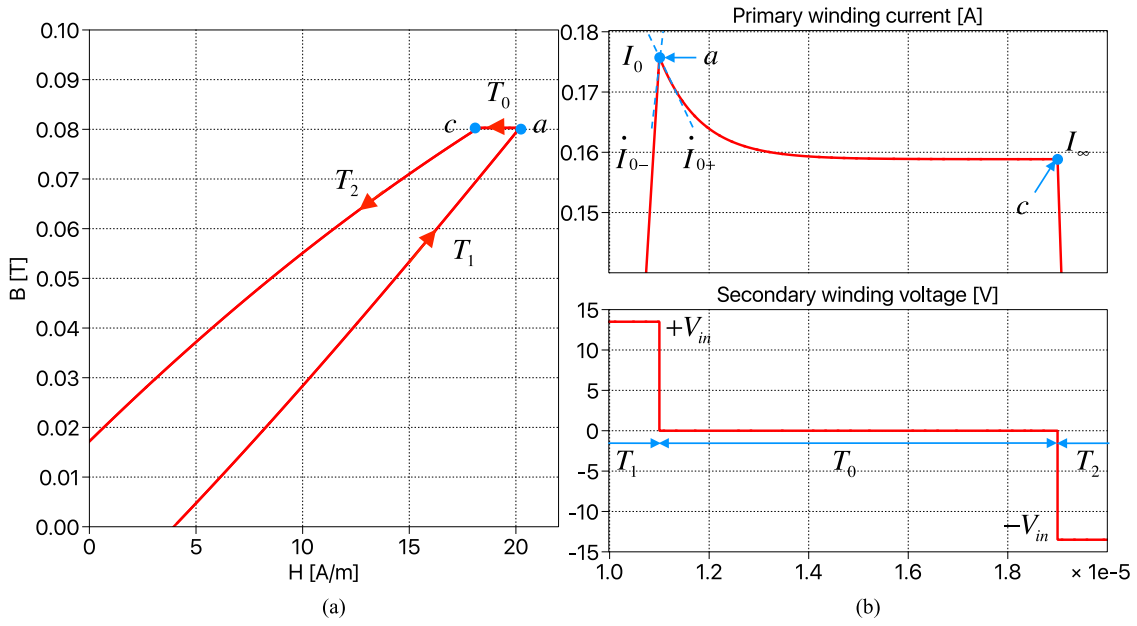


Fig. 10. Circuit behavior of the proposed model in reproducing the relaxation effect. (a) B - H characteristic including a flat part near the peak (from point a to c). (b) Time-domain waveform with current descending rapidly at the beginning of the zero-voltage period.

changing rate $\dot{\Phi} = d\Phi/dt$) governed by the following equation:

$$F = R_m \cdot \dot{\Phi}. \quad (5)$$

Please note that there is no magnetic resistor placed at the left-hand side of the hysteresis permeance, which was present in the structure proposed by [23] mainly accounting for the eddy current effect. This complies to the fact that we neglect the eddy current effect of ferrite materials, which has negligible contribution to the core loss, compared to the relaxation effect and frequency-independent hysteresis. It is also to be emphasized that if sufficiently low-frequency sinusoidal excitation is applied, R_m has negligible effect and the B - H characteristic of the overall system is equal to that of the original \mathcal{P}_1 (since the summation of \mathcal{P}'_1 and \mathcal{P}_2 is equal to \mathcal{P}_1), as the symmetrical loops within the range $[-\hat{H}, +\hat{H}]$ as demonstrated in Fig. 9. If the excitation is high-frequency PWM especially with zero-voltage period, the relaxation effect taking place in reality

can be covered by R_m . In the next step, the mechanism of the relaxation effect is interpreted in the magnetic circuit. We still take the simplified circuit model of the test setup in Fig. 7(a) as example, with the original permeance block proposed in [10] extended to the new structure. The circuit resistance and winding resistance are neglected. The time area in which the external excitation (generated via switching the T-shaped bridge) varies from positive to negative (including the zero-voltage period in between) is analyzed, and the dc voltages V_3 and V_4 are assumed to be tuned (equal to $\pm V_{in}$) so that the equivalent field strength is controlled in the range $[-\hat{H}, +\hat{H}]$.

- 1) Period T_1 : When the switch Q_1 is turned ON, positive voltage $+V_{in}$ is applied to the primary winding and the circuit current rises, as the interval T_1 in Fig. 10(b) demonstrates. In the permeance-capacitor-based magnetic circuit, the voltage excitation is translated as a “magnetic” current source (flux rate $\dot{\Phi} = V_{in}/N$), which charges the

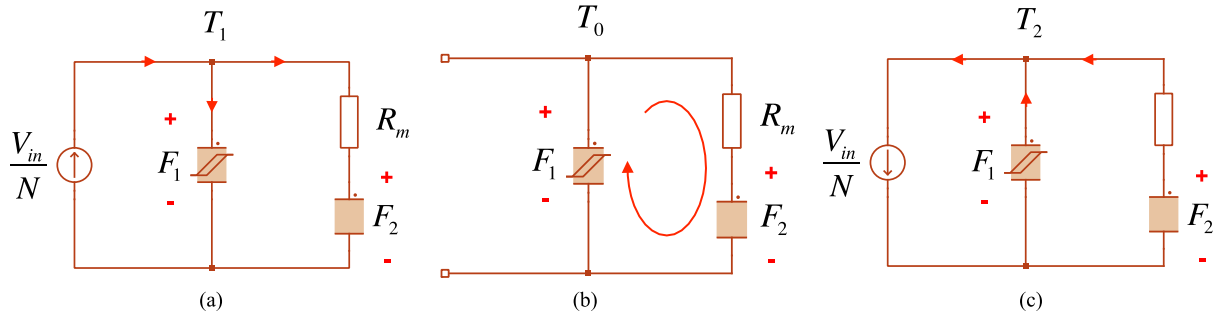


Fig. 11. Equivalent circuit configuration. (a) Positive excitation. (b) Zero-voltage period. (c) Negative excitation.

two permeance capacitors \mathcal{P}'_1 and \mathcal{P}_2 , as demonstrated in Fig. 11(a). The “magnetic” voltage (MMF denoted as F_1) of permeance \mathcal{P}'_1 increases, which leads to increased equivalent field strength, as shown in Fig. 10(b) (rising interval T_1). The equivalent field strength seen from the excitation source is given by

$$H = F_1/l \quad (6)$$

where l is the equivalent magnetic path length of the core. Under the positive excitation, the MMF of \mathcal{P}_2 (denoted as F_2) also increases, however, in a slower rate due to the existence of the resistor R_m . This leads to the fact that at the end of period T_1 [point a in Fig. 10(a)], $F_{2,0}$ is lower than $F_{1,0}$. The rising rate $\dot{F}_{1,0-} = dF_1/dt(0_-)$ directly before point a is given as follows:

$$\dot{F}_{1,0-} = \frac{l}{(\mu_{1,\uparrow} - \mu_2) \cdot A} \cdot \left(\frac{V_{in}}{N} - \frac{F_{1,0} - F_{2,0}}{R_m} \right). \quad (7)$$

In the above equation, A is the cross-sectional area of the core sample and N is the primary winding’s turns number. $\mu_{1,\uparrow}$ is the ascending permeability of the original frequency-independent model at the peak $H = \hat{H}$ (see Fig. 9). The peak MMF ($F_{1,0}$) and the rising rate ($\dot{F}_{1,0-}$) can be determined from the peak primary winding current I_0 and its rising rate \dot{I}_{0-} using the following equation:

$$F_{1,0} = I_0 \cdot \frac{l}{N}, \quad \dot{F}_{1,0-} = \dot{I}_{0-} \cdot \frac{l}{N}. \quad (8)$$

- 2) Period T_0 : After the switch Q_1 is turned OFF and Q_{01} and Q_{02} is turned on, zero voltage is applied to the primary winding. In the magnetic circuit, this situation corresponds to an open circuit on the winding side, as demonstrated in Fig. 11(b). Starting from point a , there is only a circulating “magnetic” current (flux rate) flowing in the loop composed of \mathcal{P}'_1 and \mathcal{P}_2 . Due to the higher initial MMF on \mathcal{P}'_1 , the circulating “magnetic” current charges \mathcal{P}_2 and discharges \mathcal{P}'_1 , and the initial value of the MMF’s falling rate immediately after the zero-voltage period starts is given by

$$\dot{F}_{1,0+} = \dot{I}_{0+} \cdot \frac{l}{N} = \frac{l}{(\mu_{1,\downarrow} - \mu_2) \cdot A} \cdot \frac{F_{2,0} - F_{1,0}}{R_m} \quad (9)$$

where $\mu_{1,\downarrow}$ is the descending permeability of the original frequency-independent model at the peak $H = \hat{H}$ (see Fig. 9). Afterward, on the one hand, \mathcal{P}'_1 is discharged and F_1 falls down, which is reflected by the decreasing equivalent field strength in Fig. 10(a) (from point a to c). Since the flux rate out of the winding side is zero, the equivalent flux density remains unchanged. On the other hand, \mathcal{P}_2 is charged up and the MMF of both permeances gradually approach a common value. This behavior complies to the explanation of the relaxation effect given in [1] that a new thermal equilibrium is gradually achieved where the system has minimum magnetic energy state (the magnetic energy stored in the permeance capacitors is reflected by the MMF). Please note that after the MMF of the two permeances is balanced, the total energy stored is lower than that at the beginning of the zero-voltage period, and the energy difference is actually burned by the magnetic resistor R_m , which generates extra core loss. After sufficiently long time [e.g., point c in Fig. 10], following similar law of series connected electrical capacitors, the balanced MMF F_∞ fulfills the following relation:

$$\frac{\mu_2 \cdot A}{l} \cdot (F_{2,0} - F_{1,0}) = \frac{\mu_{1,\downarrow} \cdot A}{l} \cdot (F_\infty - F_{1,0}). \quad (10)$$

F_∞ can be derived from the stabilized current I_∞ [denoted in Fig. 10(b)] as $F_\infty = I_\infty \cdot N/l$.

- 3) Period T_2 : Negative voltage appears on the primary winding when the switch Q_2 is turned ON at point c in Fig. 10(b), which corresponds to a flux rate source in the magnetic circuit flowing in the opposite direction compared to that in the period T_1 , as demonstrated in Fig. 11(c). From then on, both field strength and flux density decrease rapidly as shown in Fig. 10(a). Also that after this negative voltage period, there is another zero-voltage interval T_0 coming and the situation is similar as discussed previously, however with the relaxation effect observable at the negative peak $-\hat{H}$.

B. Parameter Identification

Up to this stage, if we substitute the slopes \dot{I}_{0-} and \dot{I}_{0+} , the peak current I_0 , and the stabilized current I_∞ by the corresponding values from the measurement results [e.g., that in

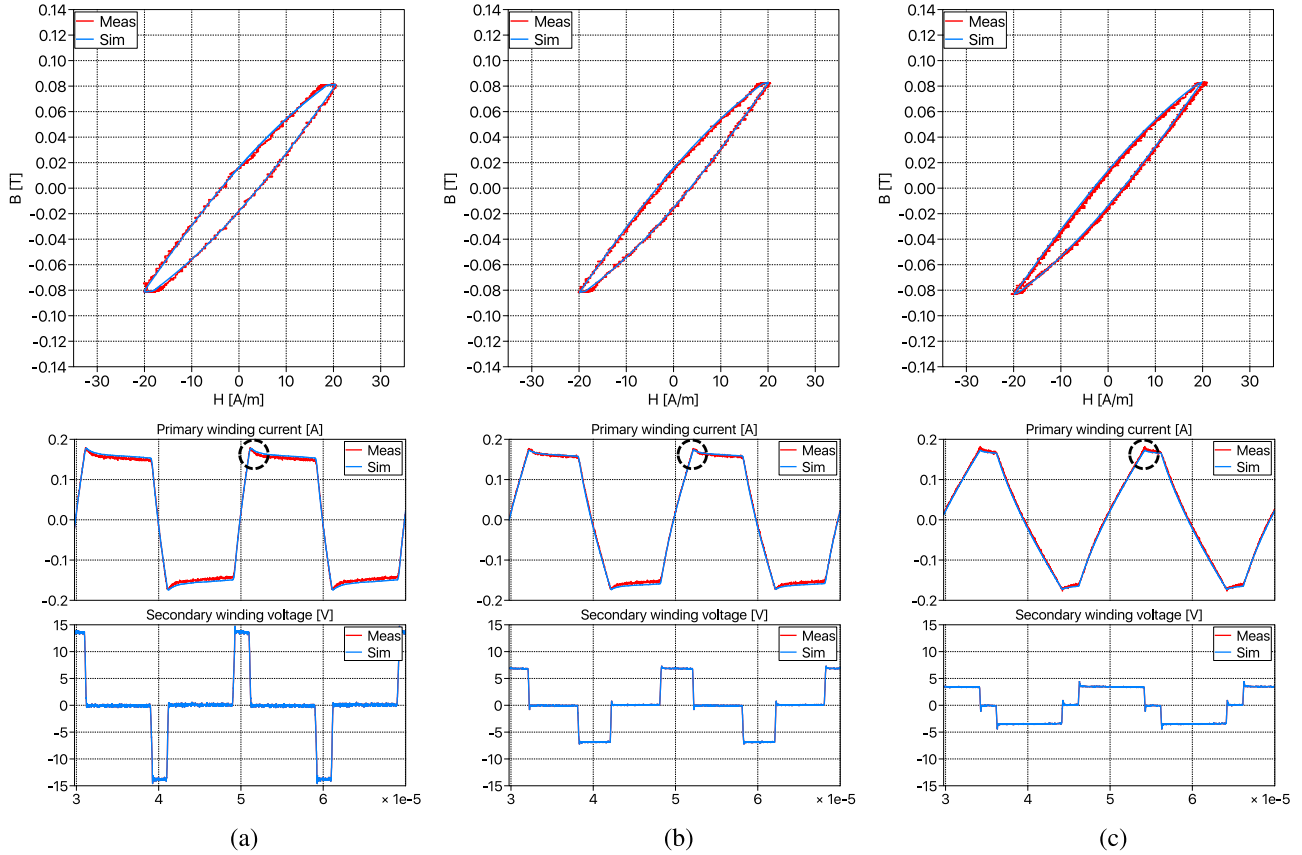


Fig. 12. B - H characteristic and time-domain waveform comparison between measurement and simulation under 50-kHz PWM excitation with peak field strength $\hat{H} = 20$ A/m and different percentages of zero-voltage period T_0 (a) 80%, (b) 60%, and (c) 20%.

Fig. 5(b)], as well as the permeabilities $\mu_{1,\downarrow}$ and $\mu_{1,\uparrow}$ by that measured under low-frequency sinusoidal excitation (with the same peak field strength), (7), (9), and (10) can be solved for R_m , μ_2 , and $F_{2,0}$. Thus, all parameters of the extended model can be explicitly determined. With μ_2 and the geometry of the core sample, \mathcal{P}_2 is calculated as follows:

$$\mathcal{P}_2 = \frac{\mu_2 \cdot A}{l}. \quad (11)$$

The measurement results for parameter identification need to be taken with the highest switching frequency and longest zero-voltage period of concern, where the relaxation effect can be obviously observed. In Section IV, it is proved that the parameterized model is able to reproduce the material's behavior at any lower switching frequency and shorter zero-voltage period.

Also please note that in the real test setup, the circuit resistance leads to the fact that the current damped down slowly after the active interval of the relaxation effect, rather than stabilized on a final value I_∞ , as the part between point b and c in Fig. 5(b) indicates. The time point b when flux starts to decrease can be identified in the measured corresponding B - H plot [in Fig. 5(a)], which indicates that the active period of the relaxation effect is over. In this case, the current at point b should be considered as I_∞ for parameter identification.

IV. EXPERIMENTAL VERIFICATION

In this section, several verification schemes of the proposed model are carried out using the test setup introduced in Section II. The ferrite material N87 is considered as the first study case with the toroidal core of shape code “R 20.0 × 10.0 × 7.00” as sample. The model is parameterized following the process from Section III-B, which is composed of two steps.

- 1) Parameters of the frequency-independent effect (model proposed in [10]) are identified using experimental measurement under sinusoidal excitation of 500 Hz, where the frequency-dependent effect is negligible.
- 2) Parameters of the relaxation effect (\mathcal{P}_2 and R_m) are identified using experimental measurement under 50-kHz PWM excitation with 80% zero-voltage period, where the amplitudes of the dc sources are trimmed to obtain peak field strength amplitude equal to $\hat{H} = 20$ A/m. The resulted parameters are $\mathcal{P}_2 = 3.18 \cdot 10^{-7}$ H and $R_m = 3.03 \Omega^{-1}$.

The circuit model is established in system-level simulation software PLECS complying to the test setup, with the same structure shown in Fig. 7(a). In order to exclude the influence of the circuit resistance of the test setup, the equivalent voltage source connected to the primary winding is fed with the measured secondary voltage multiplied by N_1/N_2 , where

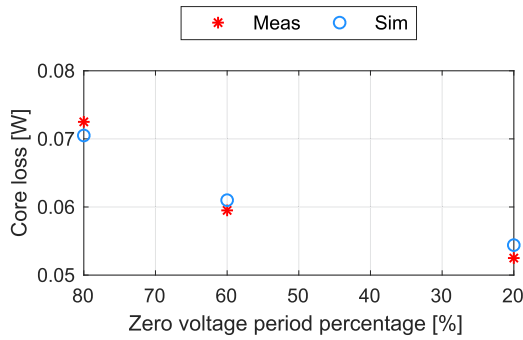


Fig. 13. Core loss comparison between measurement and simulation under 50-kHz PWM excitation with peak field strength $\hat{H} = 20$ A/m and different percentages of T_0 .

$N_1 = N_2 = 5$ are the turns number of the primary and secondary windings, respectively.

A. Verification Under PWM Excitation With Different Zero-Voltage Periods

In the first group of verification schemes, the fidelity of the proposed model is verified under $f_{sw} = 50$ kHz PWM excitation with different percentages of zero-voltage period (80%, 60%, and 20%), whereas the dc voltage sources are adjusted to maintain the equivalent peak field strength $\hat{H} = 20$ A/m. As demonstrated in Fig. 12, with decreasing percentage of zero-voltage period, the flat part near the peak of the B - H loops becomes narrower, which results in decreasing per-cycle energy loss (loop area), and indicates that the contribution from the relaxation effect reduces. The proposed model is able to reproduce the hysteresis loop with good accuracy, and the corresponding core loss power is compared to measurement in Fig. 13, and the error turns out to be under 5%. The presence of the relaxation effect is also clearly reflected on the time-domain waveform, where the primary winding current sinks with a different steepness immediately after the zero-voltage period begins, as has been highlighted by dashed circles. In the simulation model, the frequency-independent core loss (magnetic hysteresis loss) can be easily extracted by multiplying F and $\dot{\Phi}$ of the permeance \mathcal{P}'_1 and then integrating over one switching period and scaled by the switching frequency

$$P_{loss,hyst} = f_{sw} \cdot \int_T F \cdot \dot{\Phi} \cdot dt. \quad (12)$$

Subtracting the frequency-independent part from the simulated total loss, the frequency-dependent part due to relaxation effect can be directly obtained, as demonstrated in Table I. With decreasing percentage of the zero-voltage period, the frequency-dependent core loss reduces, whereas the frequency-independent one remains the same.

Afterward, the frequency of the PWM excitation is reduced to 25 kHz, whereas the dc voltage sources are configured so that the equivalent peak field strength remains at $\hat{H} = 20$ A/m. The time-domain simulation results from the same model with

TABLE I
LOSS SPLITTING OF THE SIMULATION MODEL INTO FREQUENCY-INDEPENDENT AND DEPENDENT PARTS [W]

T_0 in percentage	80%	60%	20%
Total loss	0.071	0.061	0.054
f_{sw} independent loss	0.045	0.045	0.045
f_{sw} dependent loss	0.026	0.016	0.009

90%, 60%, and 20% zero-voltage periods (longer than that in 50-kHz case) are compared to the measurement in Fig. 14, whereas the core loss powers are compared in Fig. 15. Good match is achieved here as well. One should notice that the hysteresis loop under 25-kHz excitation with 90% zero-voltage period has almost the same shape as that under 50-kHz excitation with 80% zero-voltage period, and the core loss power of the latter is two times of the former. This relation indicates that the per-cycle energy loss is the same, which has also been observed by Muehlethaler *et al.* [4]. This can be ascribed to the fact that the amplitude and duration of the nonzero (positive or negative) voltage excitation are the same in these two cases, whereas the zero-voltage phases are both long enough, so that the new thermal equilibrium can be completed re-established after the relaxation process (permeance capacitors fully recharged) and the same amount of excessive energy loss is burned.

B. Verification Under PWM Excitation With Different Duty Cycles

In multiple existing publications, significantly larger core loss was reported under strongly asymmetrical PWM excitation than that with 50% duty cycle, which can be ascribed to the frequency-dependent effect of ferrite materials. In the second group of verification schemes, 50-kHz PWM excitation with different duty cycles $d = 10\%, 20\%$, and 50% (without zero-voltage period) is applied to the same core sample. The dc voltage sources are configured following the constraint $V_3 = (1 - d) \cdot V_4$ so that the symmetrical hysteresis loop with equivalent peak field strength $\hat{H} = 20$ A/m can be obtained. The B - H characteristic and time-domain waveforms are compared between the simulation result and the experimental measurement in Fig. 16.

In comparison to the result under the symmetrical PWM excitation shown in Fig. 16(c), the top-right corner of the B - H loop under 10% duty cycle PWM in Fig. 16(a) is obviously blunter, which adds up to the loop area. This phenomenon arises from the fact that the amplitude of the positive voltage (V_3) is significantly higher than that of the negative one (V_4), and the situation at the positive-to-negative transition is similar to the positive-to-zero transition under PWM excitation with zero-voltage period so that the relaxation effect is taking place with considerable strength. In the case of symmetrical PWM excitation ($d = 50\%$) however, the material is demagnetized at the same rate as it was magnetized so that the relaxation effect has nearly no time to

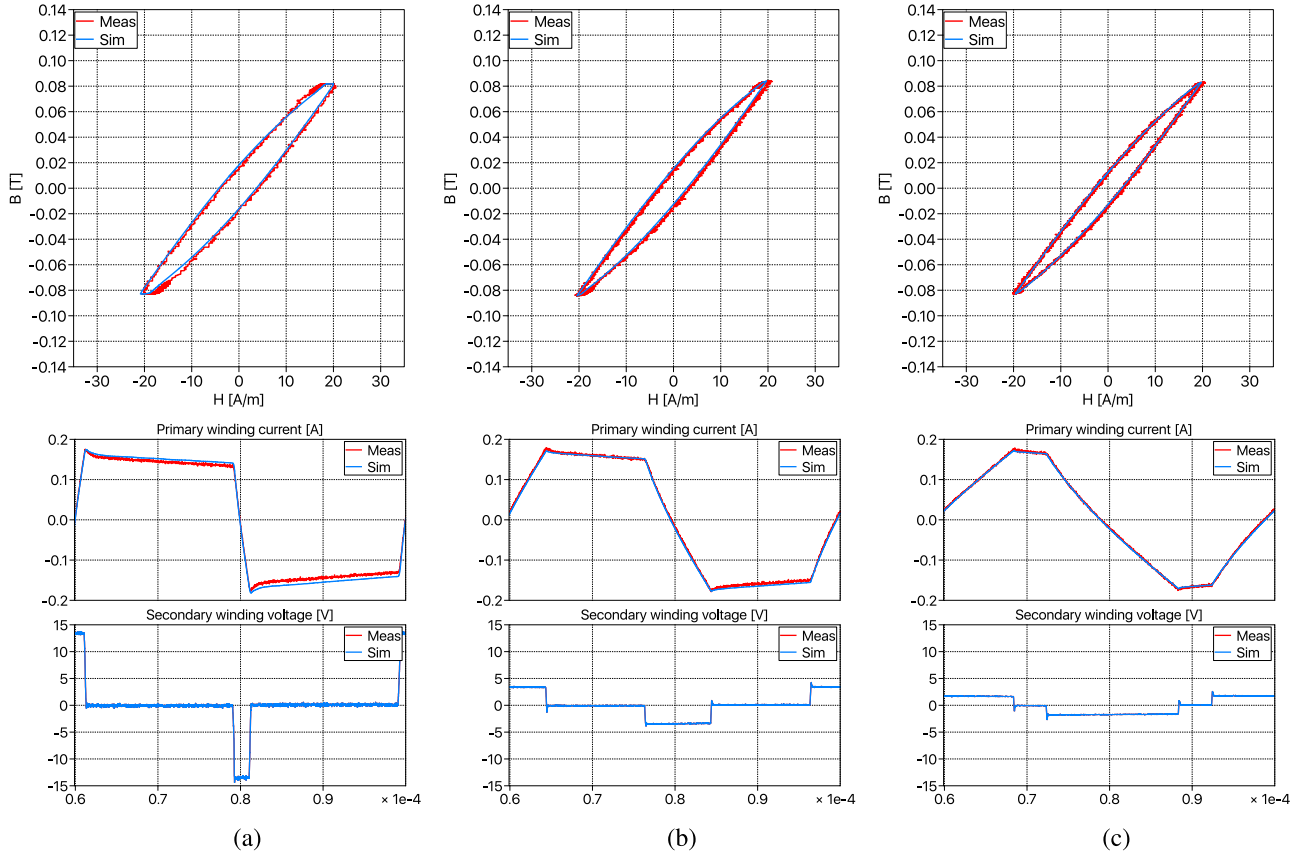


Fig. 14. B - H characteristic and time-domain waveform comparison between measurement and simulation under 25-kHz PWM excitation with peak field strength $\hat{H} = 20$ A/m and different percentages of zero-voltage period T_0 (a) 90%, (b) 60%, and (c) 20%.

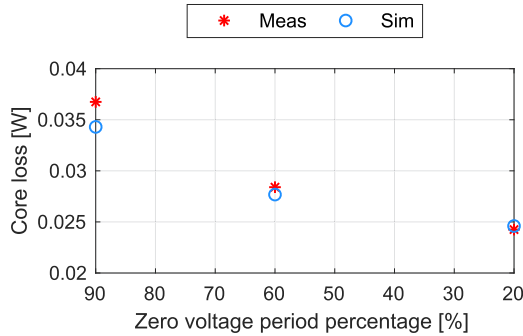


Fig. 15. Core loss comparison between measurement and simulation under 25-kHz PWM excitation with peak field strength $\hat{H} = 20$ A/m and different percentages of T_0 .

re-establish the new thermal equilibrium. Using the magnetic circuit in Fig. 11, this can be intuitively interpreted as: although \mathcal{P}'_1 is charged to higher F than \mathcal{P}_2 after the positive excitation, it is rapidly discharged afterward and its F sinks toward that of \mathcal{P}_2 in such a short time that very less energy can be burned on R_m . All the aforementioned phenomena have been captured by the proposed model both qualitatively and quantitatively, good match has been obtained in B - H characteristic and time-domain waveform shown in Fig. 16 and the core loss shown in Fig. 17.

C. Verification Under PWM Excitation With Different Amplitudes

In the third group of verification schemes, the core sample is still excited by 50-kHz PWM excitation with inclusion of zero-voltage period, and the dc voltage sources are configured to generate B - H loops with higher equivalent peak field strength $\hat{H} = 30$ A/m. Please note that in this case, the parameters of \mathcal{P}_2 and R_m are reidentified making use of the slopes \dot{I}_{0-} and \dot{I}_{0+} and the currents I_0 and I_∞ measured under 80% zero-voltage period and the permeabilities $\mu_{1,\downarrow}$ and $\mu_{1,\uparrow}$ by that measured under low-frequency sinusoidal excitation, with equivalent peak field strength $\hat{H} = 30$ A/m. The resulted values are $\mathcal{P}_2 = 5.34 \cdot 10^{-7}$ H and $R_m = 2.19 \Omega^{-1}$. The simulated B - H loops and time-domain waveforms with different zero-voltage periods are compared to that from experimental measurements in Fig. 18, and the core loss powers are compared in Fig. 19, again the proposed model is able to achieve good accuracy.

In order to accommodate the model to arbitrary amplitude of excitation, \mathcal{P}_2 and R_m need to be realized as piecewise-linear variables with the value on the supporting points identified by \dot{I}_{0-} , \dot{I}_{0+} , I_∞ , $\mu_{1,\downarrow}$, and $\mu_{1,\uparrow}$ measured under the corresponding amplitudes of excitation (with sufficiently long zero-voltage period). The modified structure of the model is demonstrated in Fig. 20, where the piecewise-linear relation between the

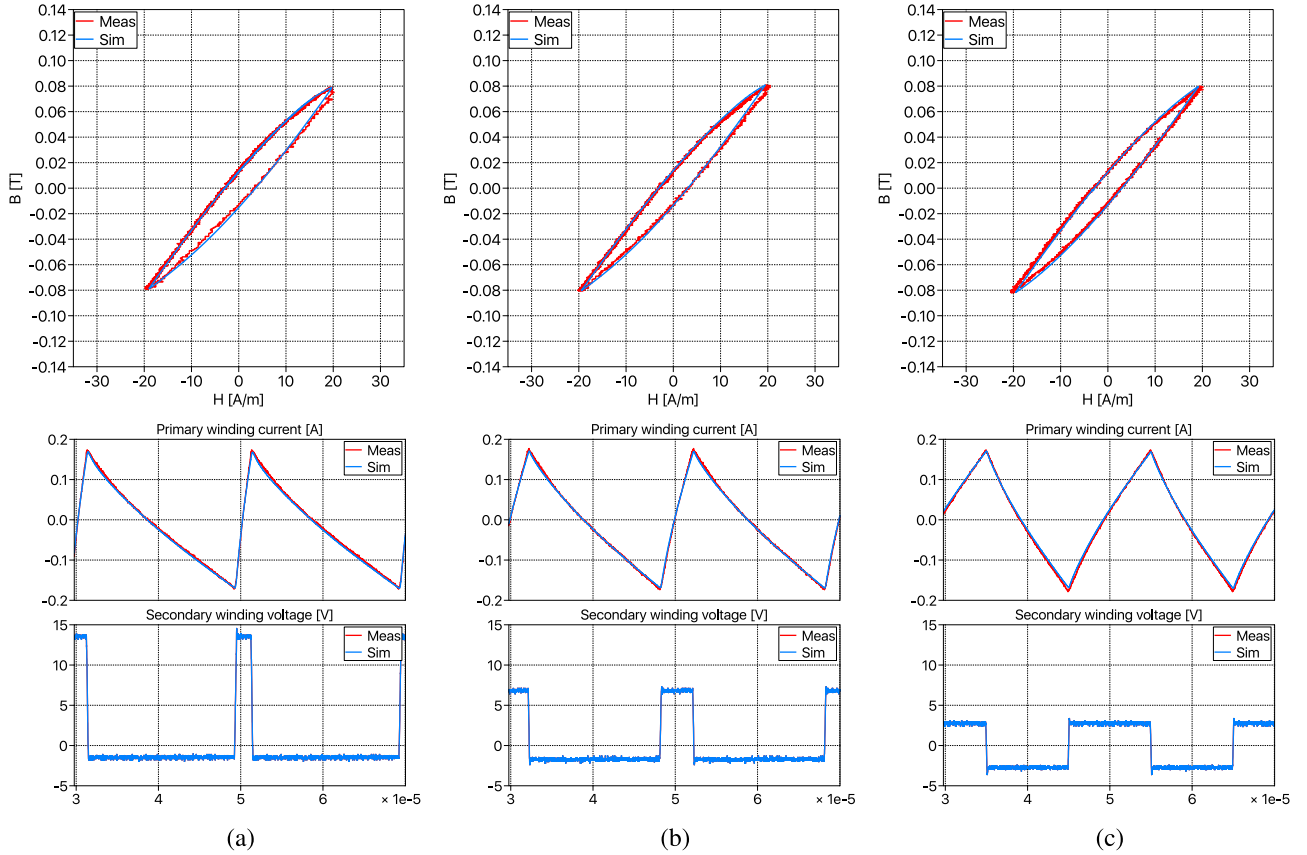


Fig. 16. B - H characteristic and time-domain waveform comparison between measurement and simulation under 50-kHz PWM excitation with peak field strength $\hat{H} = 20$ A/m and different duty cycles (a) 10%, (b) 20%, and (c) 50%.

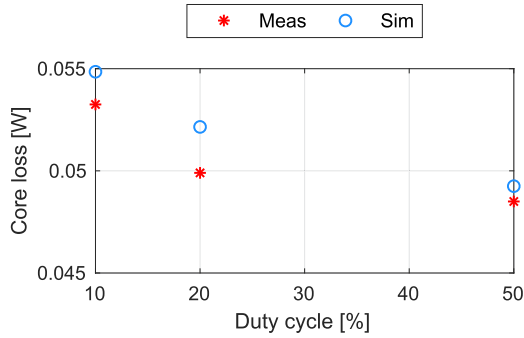


Fig. 17. Core loss comparison between measurement and simulation under 50-kHz PWM excitation with peak field strength $\hat{H} = 20$ A/m and different duty cycles.

equivalent field strength and the permeance and magnetic resistor values are included in the $f(u)$ function block, with the measured MMF of the permeance \mathcal{P}'_1 as an input.

D. Verification Under PWM Excitation With DC Offset

Using the model structure proposed in Fig. 20, arbitrary hysteresis loop inside the field strength range $H \in [-30, +30]$ A/m can be represented, even with dc bias. For verification, a differential component ΔV_{dc} is introduced into the voltage reference

of the power amplifiers V_3 and V_4 , that is

$$V_3 = V_{dc} + \Delta V_{dc}, \quad V_4 = V_{dc} - \Delta V_{dc}. \quad (13)$$

Due to the existence of circuit resistance on the primary side, the differential component ΔV_{dc} is able to stabilize the hysteresis loop at desired field strength offset. Adjusting both V_{dc} and ΔV_{dc} , the biased hysteresis loop in the field strength range $H \in [0, +30]$ A/m is obtained under different percentages of zero-voltage period. The simulation result is compared to the measurement in Fig. 21, where the B - H characteristic exhibits slight asymmetry and is captured by the simulation model. The core loss comparison in Fig. 22 also provides good match. The trend that with shorter zero-voltage period the core loss decreases is also valid for the biased loop. Observable discrepancy of the loop shape is present in Fig. 21(c), where the relaxation effect has minor impact and the frequency-independent hysteresis loss dominates, due to the fact that the static hysteresis model is not particularly parameterized taking biased loops into account. Still thanks to the physics-based property of the Preisach model, as acceptable accuracy of the biased loop is still achieved. Also please pay attention that the flux density of the biased loop depends on the historical premagnetization in reality, which cannot be explicitly measured in the existing test setup. Therefore, in the B - H plots of Fig. 21, the B range is displayed centered at zero (as integration of the secondary winding voltage).

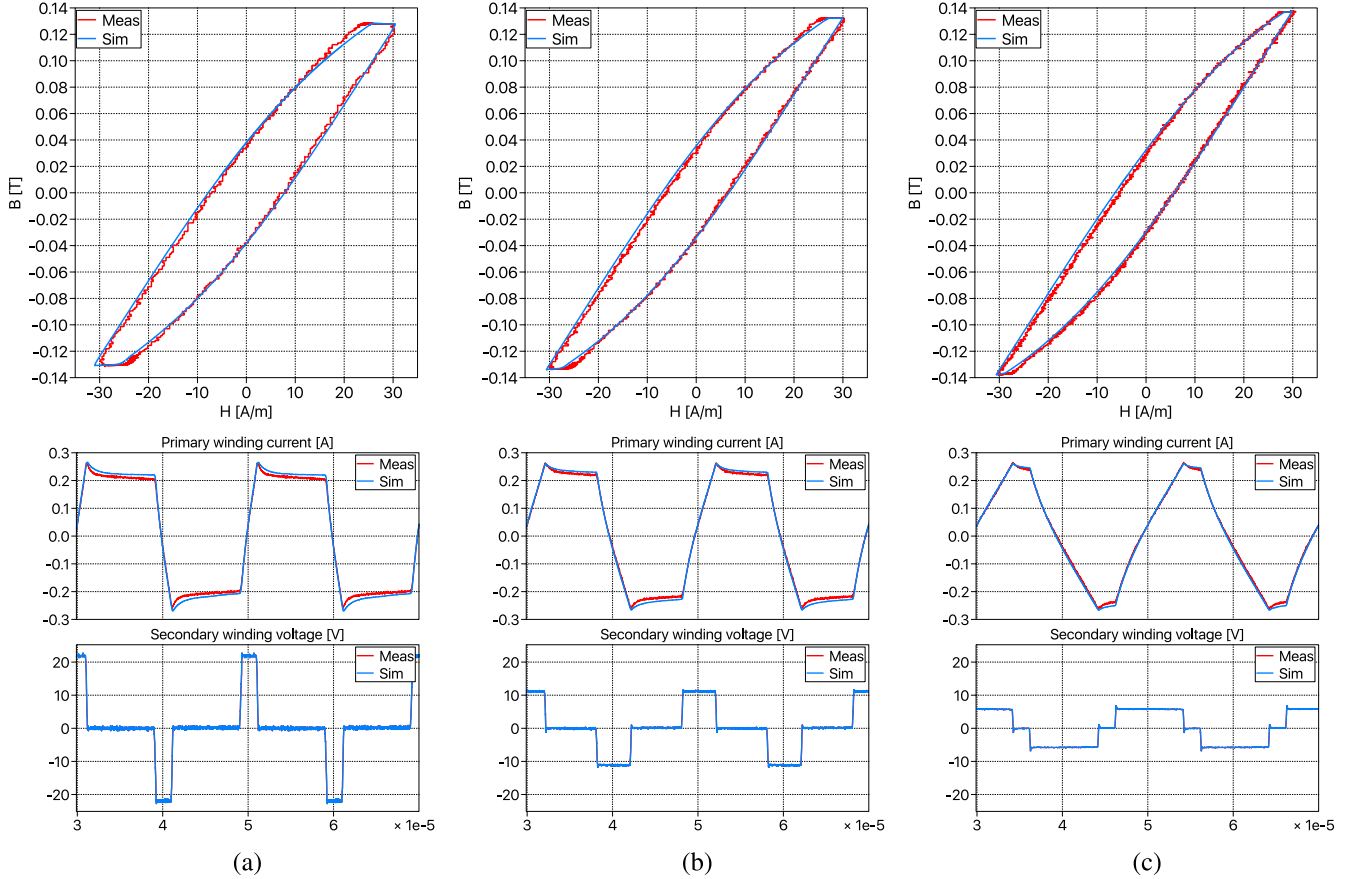


Fig. 18. B - H characteristic and time-domain waveform comparison between measurement and simulation under 50-kHz PWM excitation with peak field strength $\hat{H} = 30$ A/m and different percentages of zero-voltage period T_0 (a) 80%, (b) 60%, and (c) 20%.

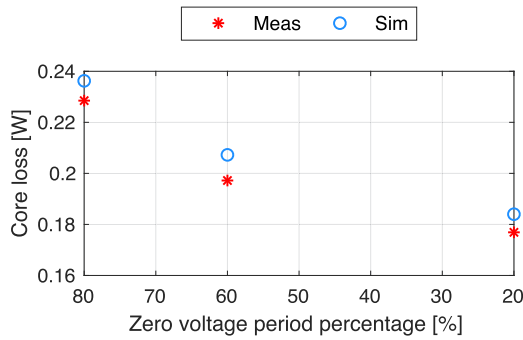


Fig. 19. Core loss comparison between measurement and simulation under 50-kHz PWM excitation with peak field strength $\hat{H} = 30$ A/m and different percentages of zero-voltage period T_0 .

E. Verification on Core Sample With Different Geometries

Once the parameters of the frequency-independent hysteresis and the frequency-dependent relaxation effect are identified using one core sample for certain ferrite materials, the model can be easily extended to other geometries. Assuming that the core sample for parameterization has cross-sectional area A_1 and equivalent magnetic path length l_1 , the permeances $\mathcal{P}'_{1,(2)}$, $\mathcal{P}_{2,(2)}$ and magnetic resistor $R_{m,(2)}$ of another core with other

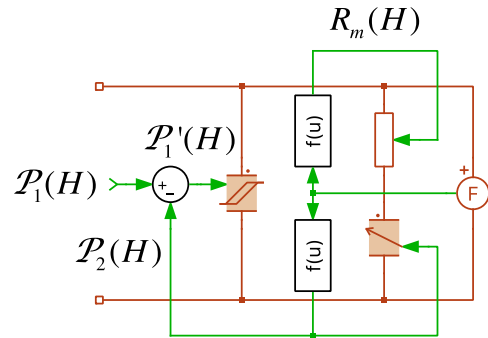


Fig. 20. Piecewise-linear realization of \mathcal{P}_2 and R_m to accommodate arbitrary amplitudes of excitation.

cross-sectional area A_2 and equivalent magnetic path length l_2 can be scaled from $\mathcal{P}'_{1,(1)}$, $\mathcal{P}_{2,(1)}$, and $R_{m,(1)}$ given as

$$\mathcal{P}'_{1,(2)} = \mathcal{P}'_{1,(1)} \cdot \frac{A_2}{A_1} \cdot \frac{l_1}{l_2} \quad (14)$$

$$\mathcal{P}_{2,(2)} = \mathcal{P}_{2,(1)} \cdot \frac{A_2}{A_1} \cdot \frac{l_1}{l_2} \quad (15)$$

$$R_{m,(2)} = R_{m,(1)} \cdot \frac{A_1}{A_2} \cdot \frac{l_2}{l_1}. \quad (16)$$

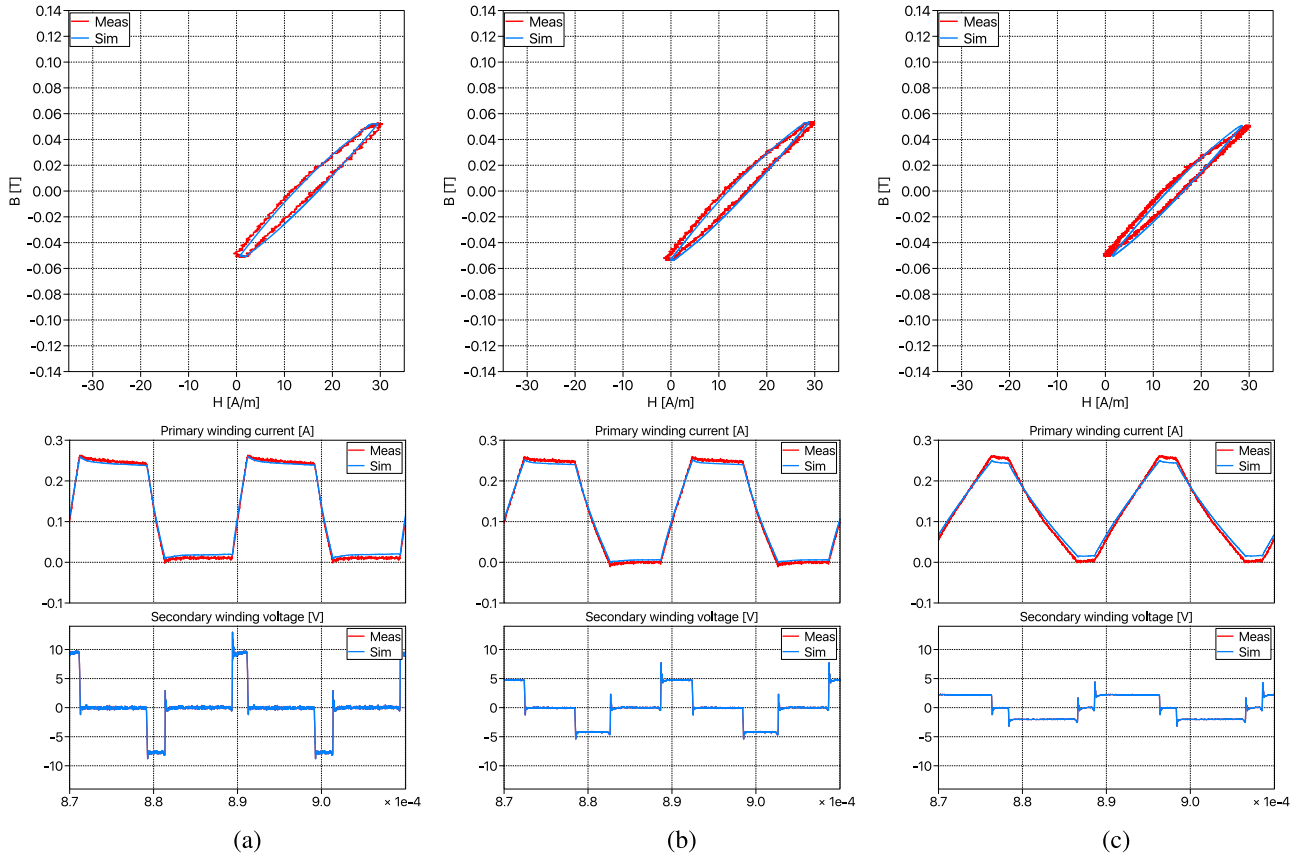


Fig. 21. B - H characteristic and time-domain waveform comparison between measurement and simulation under 50-kHz PWM excitation with biased field strength range $H \subset [0, +30]$ A/m and different percentages of zero-voltage period T_0 (a) 80%, (b) 60%, and (c) 20%.

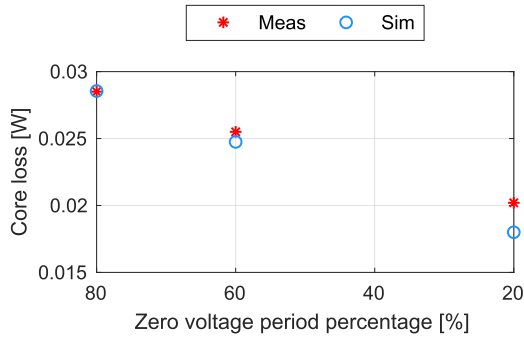


Fig. 22. Core loss comparison between measurement and simulation under 50-kHz PWM excitation with biased field strength range $H \subset [0, +30]$ A/m and different percentages of zero-voltage period T_0 .

The verification is first carried out on the toroidal core with shape code “R 25.3 \times 14.8 \times 10.0,” and the geometry difference compared to the previous core sample “R 20.0 \times 10.0 \times 7.00” is visible in Fig. 23(a). PWM excitation of 50 kHz switching frequency and different zero-voltage periods is applied, whereas the dc voltage sources are configured to obtain $\hat{H} = 20$ A/m peak equivalent field strength, which is similar to the case presented in Section IV-A. The comparison between simulated and measured core loss power is displayed in Fig. 23(b), where only small error exists. Please note that the scaling can also be

applied to the model of a complex core, where separate parts of the core are represented by a circuit of multiple permeances.

The E-core with shape code “E 20/10/6” (product number “B66311G0000X187”) is taken as the next verification case, as shown in Fig. 24(a). The circuit model is established according to the real geometry, as shown in Fig. 24(b). Each of the permeances \mathcal{P}_{c1} and \mathcal{P}_{c2} represents one single part of the core, which has the internal structure as shown in Fig. 20. The equivalent geometrical parameters (cross-section area and magnetic path length) are calculated following the formula proposed by Marxgut *et al.* [24]. All the values of \mathcal{P}'_1 , \mathcal{P}_2 and R_m for the individual permeances are scaled by the geometry of the corresponding part of the E-core from that obtained previously using the toroidal core sample, following (14)–(16). Please note that there is no new experimental measurement needed for parameterization of the core permeances \mathcal{P}_{c1} and \mathcal{P}_{c2} , where the core material characteristic is included.

Considering the accuracy limitation of the test setup in measuring gapped cores, where the phase shift Φ_{v-i} becomes close to 90° and results in extremely high $\tan(\Phi_{v-i})$ in (1), and the two E-core parts are tightly pressed together. Nevertheless, a tiny air gap still exists in between, depending on the treatment of the joining surface during the manufacturing process. The length l_g of the tiny air gap between the two E-core parts is difficult to measure, but can be estimated using the measured frequency-independent B - H characteristic of the E-core and

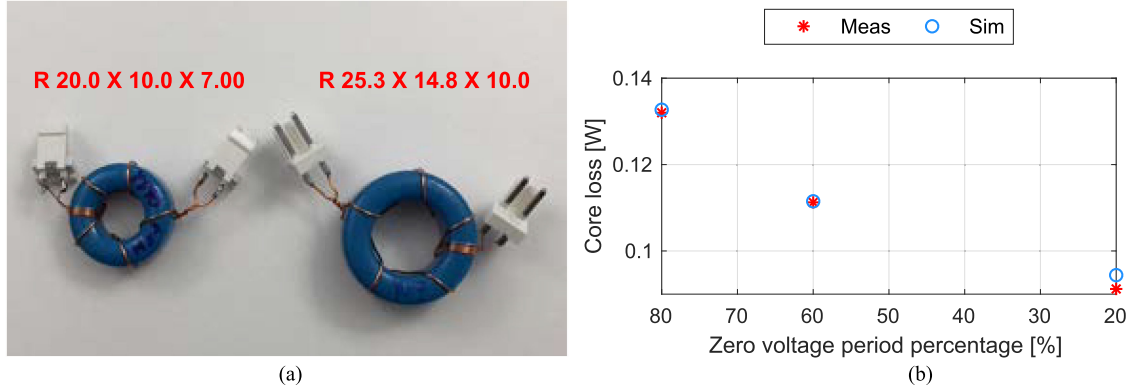


Fig. 23. (a) Core sample “R 25.3 × 14.8 × 10.0” and “R 20.0 × 10.0 × 7.00” of different geometries. (b) Core loss comparison between measurement and simulation under 50-kHz PWM excitation with peak field strength $\hat{H} = 20$ A/m and different percentages of zero-voltage period T_0 obtained from the core “R 25.3 × 14.8 × 10.0.”

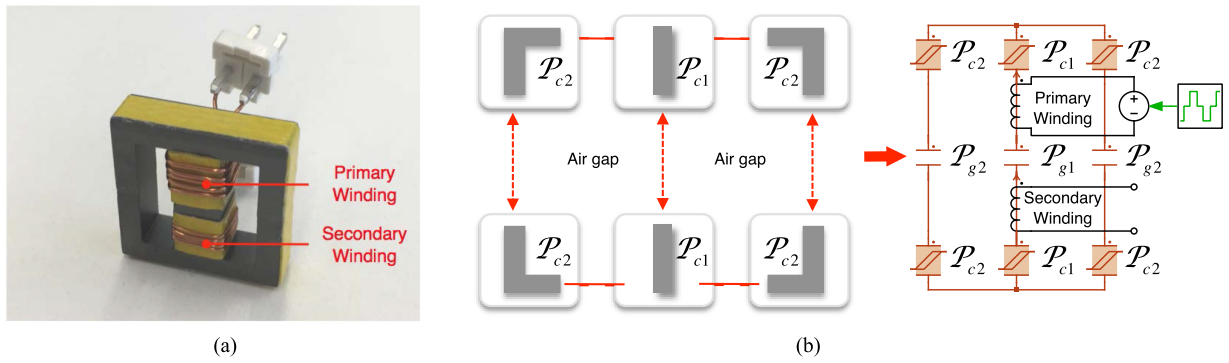


Fig. 24. (a) E-shaped core sample “E 20/10/6”. (b) Simulation model with separate permeances representing middle, side limbs and air gap of the core.

that of the toroidal core: The air gap results in different shapes of the static hysteresis loop obtained under 500-Hz sinusoidal excitation, in comparison to that of the toroidal core, as demonstrated in Fig. 25. With the same equivalent peak field strength $\hat{H} = 40$ A/m, the loop of toroidal core and E-core exhibits different equivalent permeabilities μ_{ungap} and μ_{gap} (slope of the virtual straight line connecting the two peaks), respectively. l_g can be calculated by (17). Please note that the air gap has linear B - H characteristic so that the permeance obtained in the two equations above remains constant for different operating conditions

$$l_g = \frac{1}{2} \cdot \mu_0 \cdot l_e \cdot \left(\frac{1}{\mu_{\text{gap}}} - \frac{1}{\mu_{\text{ungap}}} \right) = 4.5 \mu\text{m} \quad (17)$$

where l_e is the equivalent magnetic path length of the E-core provided by the datasheet. In the circuit model shown in Fig. 24(b), the air gap on the middle limb is represented by the constant permeance \mathcal{P}_{g1} and that on the side limbs by \mathcal{P}_{g2} . Please note that \mathcal{P}_{g1} and \mathcal{P}_{g2} have the same length l_g , whereas the cross-sectional area is configured to be the same as \mathcal{P}_{c1} and \mathcal{P}_{c2} , respectively

$$\mathcal{P}_{g1} = \mu_0 \cdot \frac{A_{c1}}{l_g}, \quad \mathcal{P}_{g2} = \mu_0 \cdot \frac{A_{c2}}{l_g}. \quad (18)$$

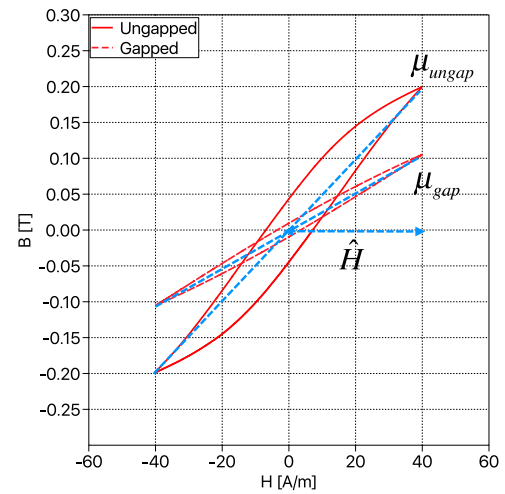


Fig. 25. B - H characteristic measured from toroidal core without air gap (peak flux density \hat{B}_{ungap}) and E-core with tiny air gap (peak flux density \hat{B}_{gap}) under 500-Hz sinusoidal excitation.

The verification is still carried out under the PWM excitation with different lengths of zero-voltage period, and the dc output voltage of V_3 and V_4 are configured to generate unbiased B - H loop with peak field strength $\hat{H} = 30$ A/m. The time-domain

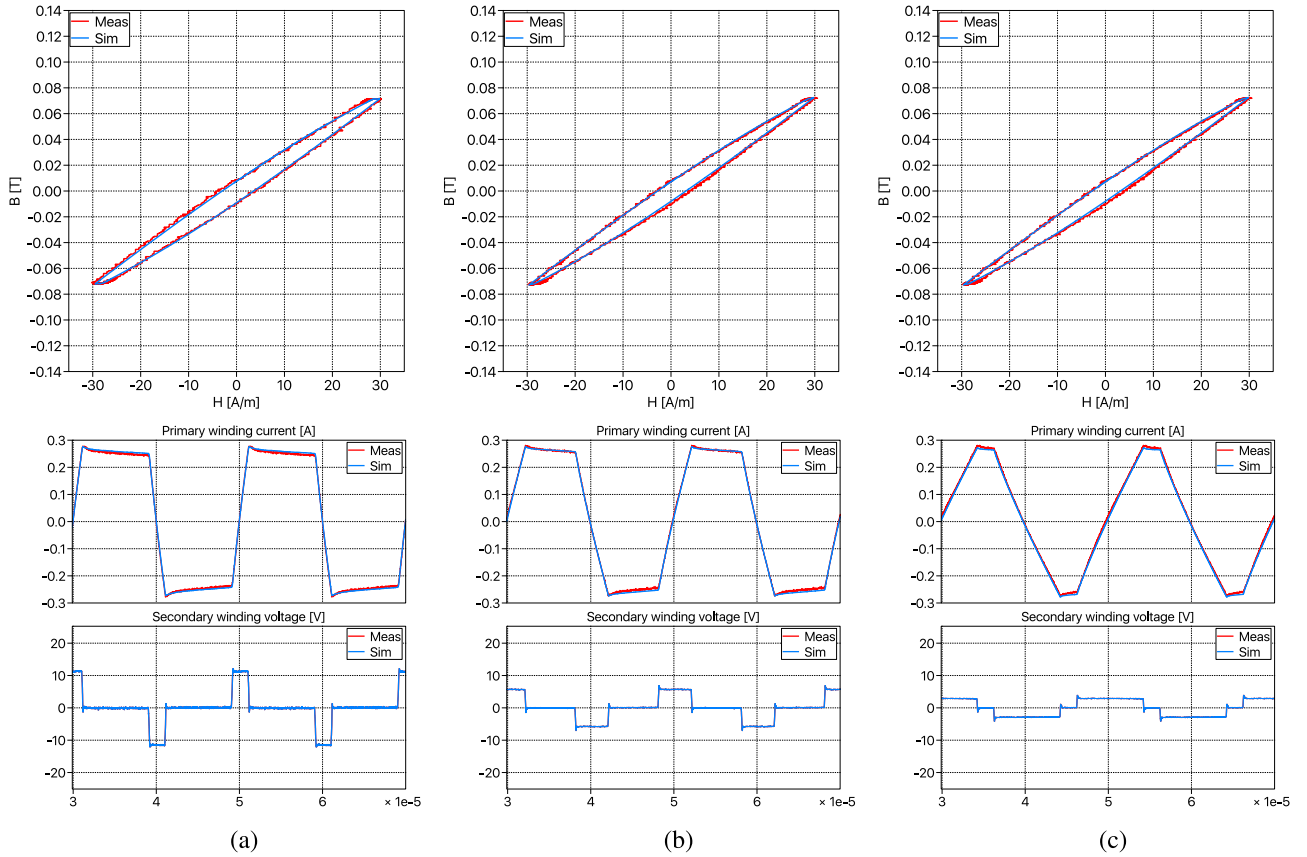


Fig. 26. B - H characteristic and time-domain waveform comparison of E-core “E 20/10/6” between measurement and simulation under 50-kHz PWM excitation with equivalent peak field strength $\hat{H} = 30$ A/m and different percentages of zero-voltage period T_0 (a) 80%, (b) 60%, and (c) 20%.

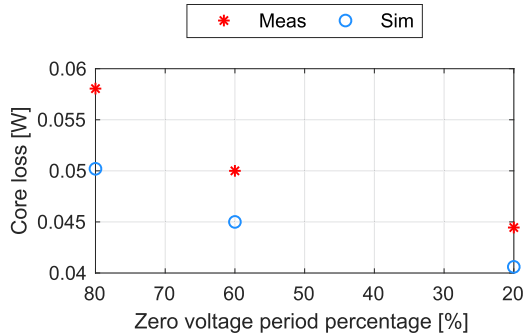


Fig. 27. Core loss comparison of E-core “E 20/10/6” between measurement and simulation under 50-kHz PWM excitation with equivalent peak field strength $\hat{H} = 30$ A/m and different percentages of zero-voltage period T_0 .

waveforms and the B - H characteristic are compared between measurement and simulation in Fig. 26. Due to the presence of the tiny air gap, the B - H characteristic has lower loop area and slope, in comparison to that of the toroidal core in Fig. 18. The influence of the zero-voltage period on the core loss is well reflected by the proposed model with maximum error of 13.5 %, as demonstrated in Fig. 27. The error is larger than in the case of the toroidal core presented in Fig. 19, which can be ascribed to the estimation error of the air gap length l_g .

F. Verification on Core Sample of Different Ferrite Materials

In the last group of verification schemes, the model is verified with another ferrite material N30 from EPCOS. The toroidal core with shape code “R 16.0 × 9.60 × 6.30” is taken as sample. Again 50-kHz PWM excitation with different zero-voltage periods is applied to the core sample, in which case, the relaxation effect can be obviously observed. The model is parameterized using the measurement with 80% zero-voltage period and peak equivalent peak field strength $\hat{H} = 20$ A/m. The resulted parameters are $\mathcal{P}_2 = 3.79 \cdot 10^{-7}$ H and $R_m = 2.43 \Omega^{-1}$, which are constant since the measurement of one field strength amplitude is taken for parameterization. The comparison between simulation and measurement regarding the B - H characteristic, and the time-domain waveform and the core loss power are presented in Figs. 28 and 29, respectively. In comparison to the ferrite material N87, the B - H loop of N30 exhibits significantly different shapes, and still, good match has been achieved by the proposed model.

This paper focuses on frequency-dependent core loss of ferrite materials, whose electrical conductivity is extremely low. In this way, the conductivity related eddy current effect can be neglected in the frequency range that has been considered (≤ 50 kHz), and the relaxation effect, which is not related to the material conductivity, can be clearly analyzed. For the other metal-based materials (e.g., metal powders or nanocrystalline),

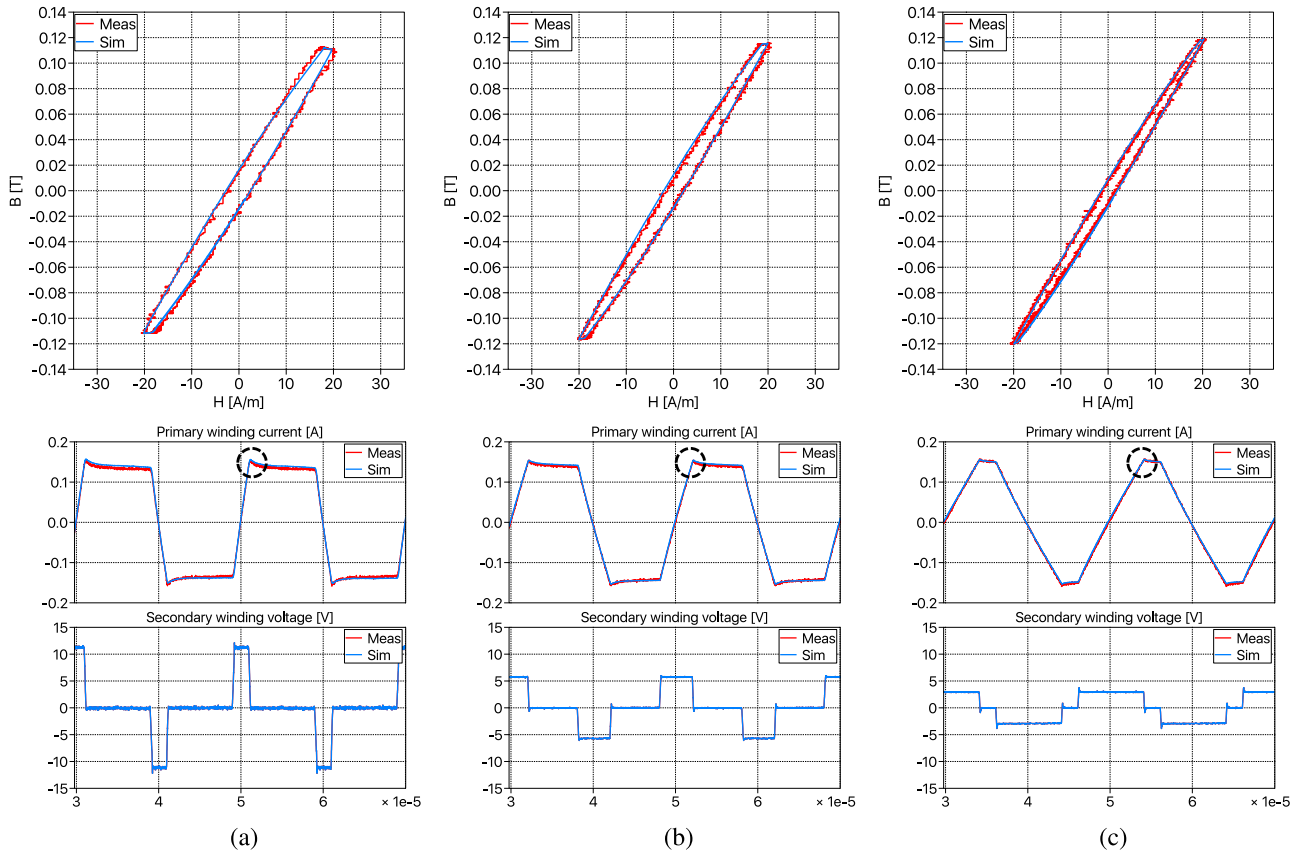


Fig. 28. B - H characteristic and time-domain waveform comparison between measurement and simulation of ferrite material N30 under 50-kHz PWM excitation with peak field strength $\hat{H} = 20$ A/m and different percentages of zero-voltage period T_0 (a) 80%, (b) 60%, and (c) 20%.

the frequency-dependent core loss can be dominated by the eddy current effect, which is however, not in the scope of this paper.

V. APPLICATION OF THE PROPOSED MODEL

One application of the proposed model is the optimization of the magnetic component, which can be carried out in an intuitive way, taking into account its desired operating condition in the target power converter system. Since the optimization method is not in the scope of this paper, only a simplified workflow is demonstrated in Fig. 30 and described as follows.

- At first, the required material characteristic under low - frequency sinusoidal and high-frequency PWM excitation is obtained using a toroidal core sample.
 - Second, the permeance model is parameterized following the procedure introduced in Section III.
 - Then, the iterative optimization of the magnetic component can be started. In each iteration, a different core geometry and turns number of the windings are chosen.
 - The permeance block is integrated into the circuit simulation environment of the target power converter system and scaled by the core geometry, according to the description in Section IV-E. Also the winding components is configured by the desired turns number. The circuit model

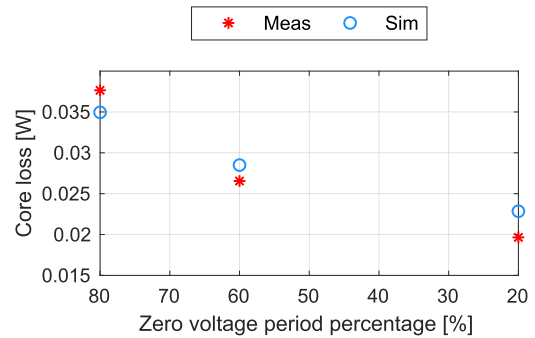


Fig. 29. Core loss comparison between measurement and simulation of ferrite material N30 under 50-kHz PWM excitation with peak field strength $\hat{H} = 20$ A/m and different percentages of zero-voltage period T_0 .

is simulated in time domain and the core loss power is obtained.

- 5) Taking the simulated core loss power and the volume of the selected core in the current iteration, a certain objective function as tradeoff between power loss and volume is evaluated.
 - 6) The output of the objective function indicates the direction to change the core geometry and winding turns number; afterward, the new core geometry and winding turns number are applied to the circuit model in the next iteration.

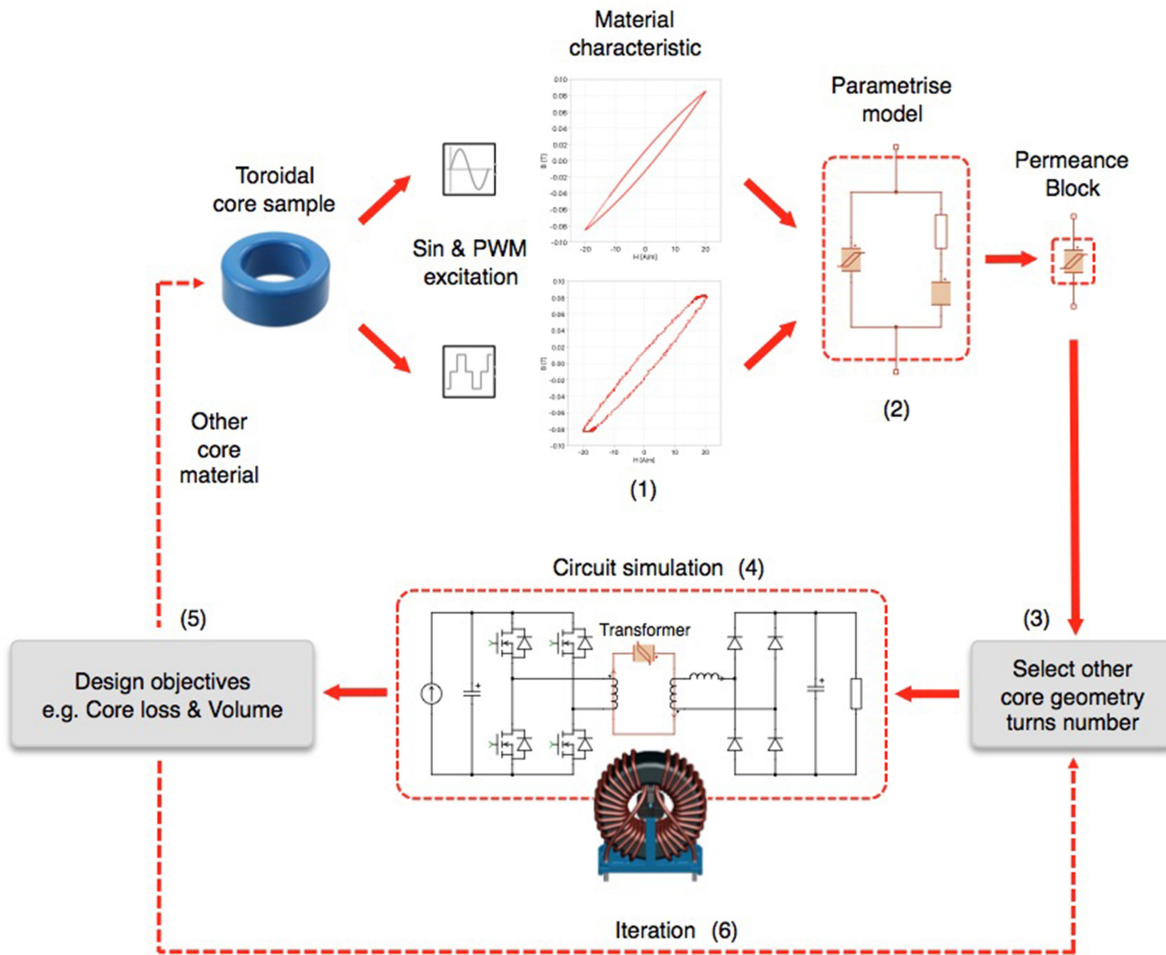


Fig. 30. Work flow using the proposed model to optimize magnetic component design.

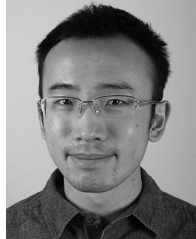
VI. CONCLUSION

This paper proposes a modeling approach for frequency-dependent core loss of ferrite core materials, which takes into account both frequency-independent magnetic hysteresis and frequency-dependent relaxation effect. The model can be seamlessly integrated into system-level circuit simulations and can be easily extended to different geometries. The fidelity of the proposed model has been verified under PWM excitations of different switching frequencies, zero-voltage period, and duty cycle. With the proposed model, the power electronic designers are able to get intuitive insight to the magnetic core loss of magnetic components using ferrite materials, in relation to the individual operating conditions. Based on the simulation result, improvement or optimization of the magnetic component itself or the power electronic circuitry can be carried out in an efficient way.

REFERENCES

- [1] J. B. Goodenough, "Summary of losses in magnetic materials," *IEEE Trans. Magn.*, vol. 38, no. 5, pp. 3398–3408, Sep. 2002.
- [2] J. Reinert, A. Brockmeyer, and R. W. A. A. D. Doncker, "Calculation of losses in ferro- and ferrimagnetic materials based on the modified Steinmetz equation," *IEEE Trans. Ind. Appl.*, vol. 37, no. 4, pp. 1055–1061, Jul./Aug. 2001.
- [3] C. R. Sullivan, J. H. Harris, and E. Herbert, "Core loss predictions for general PWM waveforms from a simplified set of measured data," *Proc. 25th Annu. IEEE Appl. Power Electron. Conf. Expo.*, 2010, pp. 1048–1055.
- [4] J. Muehlethaler, J. Biela, J. W. Kolar, and A. E. Ecklebe, "Improved core-loss calculation for magnetic components employed in power electronic systems," *IEEE Trans. Power Electron.*, vol. 27, no. 2, pp. 964–973, Feb. 2012.
- [5] S. Barg, K. Amrous, H. Mejibri, and A. Amrous, "An improved empirical formulation for magnetic core losses estimation under nonsinusoidal induction," *IEEE Trans. Power Electron.*, vol. 32, no. 3, pp. 2146–2154, Mar. 2017.
- [6] V. Basso, "Hysteresis and relaxation effects in magnetic materials," *IEEE Trans. Magn.*, vol. 36, no. 5, pp. 3176–3181, Sep. 2000.
- [7] A. Abramovitz and S. Ben-Yaakov, "RGSE-based spice model of ferrite core losses," *IEEE Trans. Power Electron.*, vol. 33, no. 4, pp. 2825–2831, Apr. 2018.
- [8] I. Mayergoyz, *Mathematical Models of Hysteresis and Their Applications*. New York, NY, USA: Academic, 2003.
- [9] J. T. Hsu and K. D. T. Ngo, "A Hammerstein-based dynamic model for hysteresis phenomenon," *IEEE Trans. Power Electron.*, vol. 12, no. 3, pp. 406–413, May 1997.
- [10] M. Luo, D. Dujic, and J. Allmelting, "Modeling frequency independent hysteresis effects of ferrite core materials using permeance-capacitance analogy for system-level circuit simulations," *IEEE Trans. Power Electron.*, early access, 2018.
- [11] J. G. Zhu, S. Y. R. Hui, and V. S. Ramsden, "A dynamic equivalent circuit model for solid magnetic cores for high switching frequency operations," *IEEE Trans. Power Electron.*, vol. 10, no. 6, pp. 791–795, Nov. 1995.

- [12] J. van Vlerken and P. G. Blanken, "Lumped modelling of rotary transformers, heads and electronics for helical-scan recording," *IEEE Trans. Magn.*, vol. 31, no. 2, pp. 1050–1055, Mar. 1995.
- [13] L. Dalessandro, W. G. H. Odendaal, and J. W. Kolar, "HF characterization and nonlinear modeling of a gapped toroidal magnetic structure," *IEEE Trans. Power Electron.*, vol. 21, no. 5, pp. 1167–1175, Sep. 2006.
- [14] D. Hamill, "Lumped equivalent circuits of magnetic components: The gyrator-capacitor approach," *IEEE Trans. Power Electron.*, vol. 8, no. 2, pp. 97–103, Apr. 1993.
- [15] J. Allmeling, W. Hammer, and J. Schönberger, "Transient simulation of magnetic circuits using the permeance-capacitance analogy," in *Proc. IEEE 13th Workshop Control Model. Power Electron.*, 2012, pp. 3–6.
- [16] F. D. Tan, J. L. Vollin, and S. M. Cuk, "A practical approach for magnetic core-loss characterization," *IEEE Trans. Power Electron.*, vol. 10, no. 2, pp. 124–130, Mar. 1995.
- [17] Y. Han, G. Cheung, A. Li, C. R. Sullivan, and D. J. Perreault, "Evaluation of magnetic materials for very high frequency power applications," *IEEE Trans. Power Electron.*, vol. 27, no. 1, pp. 425–435, Jan. 2012.
- [18] M. Mu, Q. Li, D. J. Gilham, F. C. Lee, and K. D. T. Ngo, "New core loss measurement method for high-frequency magnetic materials," *IEEE Trans. Power Electron.*, vol. 29, no. 8, pp. 4374–4381, Aug. 2014.
- [19] D. Hou, M. Mu, F. C. Lee, and Q. Li, "New high-frequency core loss measurement method with partial cancellation concept," *IEEE Trans. Power Electron.*, vol. 32, no. 4, pp. 2987–2994, Apr. 2017.
- [20] J. Muehlethaler, J. Biela, J. W. Kolar, and A. Ecklebe, "Core losses under DC bias condition based on Steinmetz parameters," *IEEE Trans. Power Electron.*, vol. 27, no. 2, pp. 953–963, Feb. 2012.
- [21] TDK, "EPCOS data book 2013: Ferrites and accessories," 2013.
- [22] [Online]. Available: <http://www.vishay.com/landingpage/extreme/2014/shunt.html>
- [23] M. Luo, D. Dujic, and J. Allmeling, "Permeance based modeling of magnetic hysteresis with inclusion of eddy current effect," in *Proc. IEEE Appl. Power Electron. Conf. Expo.*, 2018, pp. 1764–1771.
- [24] C. Marxgut, J. Muehlethaler, F. Krismer, and J. W. Kolar, "Multiobjective optimization of ultraflat magnetic components with PCB-integrated core," *IEEE Trans. Power Electron.*, vol. 28, no. 7, pp. 3591–3602, Jul. 2013.



Min Luo (M'13) was born in Beijing, China, in 1986. He received the B.S. degree in electrical engineering from Tsinghua University, Beijing, China, in 2009, and the M.S. degree in electrical power engineering from RWTH Aachen University, Aachen, Germany, in 2012. He is currently working toward the Ph.D. degree at the Power Electronics Laboratory, École Polytechnique Fédérale de Lausanne (EPFL), Lausanne, Switzerland.

Since 2012, he has been an Application Engineer with Plexim, Zurich, Switzerland, working on the software PLECS for fast simulation of power electronic systems. In 2014, he joined Power Electronics Laboratory, EPFL as an External Doctoral Research Assistant. His research interests include dynamic modeling of magnetic components and real-time HIL simulation of power converters.



Drazen Dujic (S'03–M'09–SM'12) received the Dipl.Ing. and M.Sc. degrees from the University of Novi Sad, Novi Sad, Serbia, in 2002 and 2005, respectively, and the Ph.D. degree from the Liverpool John Moores University, Liverpool, U.K., in 2008, all in electrical engineering.

From 2002 to 2006, he was a Research Assistant with the Department of Electrical Engineering, University of Novi Sad. From 2006 to 2009, he was a Research Associate with Liverpool John Moores University. From 2009 to 2013, he was a Principal

Scientist with the ABB Corporate Research Centre, Switzerland, working on the power electronics projects spanning the range from low-voltage/power SMPS in below kilowatt range to medium voltage high-power converters in a megawatt range. During 2010–2011, he was a member of a project team responsible for the development of the world's first power electronic traction transformer successfully commissioned on the locomotive. From 2013 to 2014, he was a R&D Platform Manager, responsible for ABB's largest IGCT-based medium voltage drive—ACS6000 with the ABB Medium Voltage Drives, Turgi, Switzerland. He is currently an Assistant Professor with Ecole Polytechnique Fédérale de Lausanne, Lausanne, Switzerland and the Director of the Power Electronics Laboratory. He has authored or coauthored more than 80 scientific publications and has filed 11 patents.

Prof. Dujic is an Associate Editor for the *IEEE TRANSACTIONS ON INDUSTRIAL ELECTRONICS*, the *IEEE TRANSACTION ON POWER ELECTRONICS*, and *IET Electric Power Applications*. His research interests include the design and control of advanced high-power electronics systems and high-performance drives. He was the recipient of the First Prize Paper Award by the Electric Machines Committee of the IEEE Industrial Electronics Society at IECON-2007. In 2014, he was the recipient of the Isao Takahashi Power Electronics Award for outstanding achievement in power electronics.



Jost Allmeling (S'98–M'03) was born in Hamburg, Germany, in 1972. He received the M.S. degree in electrical engineering from Aachen University, Aachen, Germany, in 1996, and the Ph.D. degree from the Swiss Federal Institute of Technology (ETH), Zurich, Switzerland, in 2001.

In 1996, he became a Research Associate with the Power Electronics Laboratory, ETH. From 2001 to 2003, he was a Postdoctoral Researcher with the Power Systems Laboratory, ETH. In 2002, he cofounded Plexim, a spin-off company from ETH Zurich that develops the software PLECS for fast simulation of power electronic systems. He is currently the Managing Director of Plexim. His research interests include simulation of power electronics, modeling electrical and mechanical components, real-time HIL simulation, and inverter control.